Granular materials: micromechanical approaches of model systems

Jean-Noël Roux

Granular materials: micromechanical approaches of model systems.

Jean-Noël Roux*

* Université Paris-Est, Laboratoire Navier, Champs-sur-Marne, France

Published as Chapter 4 in S. Mesarovic, S. Forest and H. Zbib, editors, Mesoscale Models*, CISM Courses and Lectures, vol. 587, Springer 2019, ISSN 0254-1971*

Abstract An overview is given of micromechanical approaches to the rheology of granular materials, from solidlike granular packs to large plastic strains and dense inertial flows, which essentially relies on the numerical simulation (by the "discrete element method" or DEM) of simple model systems. The main features of contact laws are presented, and then it is insisted on the importance of the geometry of disordered granular assemblies, such that some details of contact interactions are in fact often irrelevant. Some salient results, as obtained from DEM studies over the last decades, are presented about the variety of microstructures and internal states, depending on assembling processes; on elasticity and its (limited) role in quasistatic granular behavior; on plastic strains and the fondamental concept of critical states, and on its recent applications to the rheology of dense granular flows and suspensions.

1 Introduction

A wide variety of materials used in different engineering applications are granular assemblies (Andreotti et al., 2013), made of solid particles of different sizes: sands, or, more generally, soils (Mitchell and Soga, 2005), powders used in pharmaceutical industries and food processing, building materials... Grain sizes range from micrometers for very fine powders (Castellanos, 2005), verging on the colloidal realm, to meters for rockfill materials (Deluzarche and Cambou, 2006), or even larger for some asteroids (Sánchez et al., 2017). As grains are brought into contact by confining external forces, possibly supplemented by mutual attraction, solid materials are formed, which may turn into liquidlike systems depending on the applied forces. Strongly agitated systems tend to form so-called granular gases (Jaeger et al., 1996).

At the continuum level the most sophisticated modeling attempts for the behavior of solid materials were proposed in the fields of geomechanics and geotechnique (Wood, 1990; Mitchell and Soga, 2005), in which quite elaborate experimental characterizations have also been exploited (Tatsuoka, 2001; di Benedetto et al., 2003). The modeling of dense granular flows has known significant progress over the past 15 years (GDR MiDi, 2004; Jop et al., 2006; Andreotti et al., 2013).

The micromechanics and micromorphology of granular assemblies have recently gained considerable interest (Radjaï et al., 2017), and attract nowadays a large research effort, for which the practice of the numerical simulation techniques known as "discrete element methods" (DEM), the granular analog of molecular dynamics for collections of molecules or atoms, is now an essential, widespread tool (Radjaï and Dubois, 2011; O'Sullivan, 2011).

The present contribution intends to supply a short, admittedly incomplete, review of some recent advances in the understanding of some essential features of granular mechanics, in connection with their microscopic origins, at the scale of solid grains and their interactions. It essentially relies on DEM results on model materials, with occasional illustrations in two-dimensional (2D) systems; most cited results, though, pertain to three-dimensional (3D) assemblies of spherical beads, with indications on the behavior of more general grain shapes, such as polyhedra.

Despite recent progress, our understanding of the rheophysics of granular materials is still considerably less advanced than in crystalline solids like metals and alloys. Describing the microscopic interactions, defining the material state, identifying such basic features of solid materials as an elastic range... all these essential operations carried out in the mechanical modeling of materials in relation to their elementary constituents are considerably more difficult with granular materials. Some of the most advanced attempts in micromechanics are not presented here. The aim of this chapter is, rather, to describe the landscape of current investigations, with some of its main landmarks, identifying constraints for future research and supplying possible guidelines.

It is organized as follows. First, Sec. 2 discusses the basis of mechanical modeling of granular materials, the contact interactions that derive from their geometric specificity, and some essential features of their macroscopic behavior that one wishes to relate to micromechanics. Sec. 3 introduces important tools needed to connect grain-level to macroscopic mechanics; among them statistical descriptors of material state, structural mechanics notions applied to contact networks. The following parts review some results on model systems that lead to a better understanding of the material state, as resulting from the assembling process (Sec. 4); of its properties as a solid

material in quasistatic conditions (Sec. 5, dealing with the influence of the initial state, the role of elasticity, the "critical state" at large strains), and in dense flows (Sec. 6, about microstructure and constitutive modeling). Note that granular gases are not dealt with here. Sec. 7 is a brief conclusion.

2 Specificities of granular material modeling

2.1 Contact interactions and discrete degrees of freedom

One essential characteristic of granular materials, as dealt with in mechanical models, which enables their treatment by such numerical methods as DEM, involving a finite set of degrees of freedom, is that solid grains interact in contact regions which remain very small compared to their size. This is schematically illustrated in Fig. 1: solid objects only get deformed

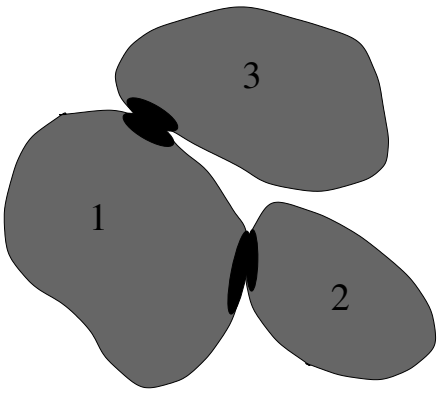

Figure 1. 3 grains, with contacts between 1 and 2, and between 1 and 3. Material strains are only notable within darker contact regions (the size of which is exaggerated to ensure visibility on the picture).

in regions close to the contacts. Outside those regions the material strains remain negligible. Those regions, shown as shaded areas in the figure, can safely be assumed to be very much smaller than the grains, and to be disjoint. The grains may thus be described as rigid, undeformable solid objects. They are merely sensitive to the total force and torque exerted on them by applied force fields (e.g., gravity) and other grains in contact with them. In Fig. 1, the force transmitted in the contact between grains 1 and 2 is only dependent on the motion of the same grains away from the contact region, where rigid body kinematics applies. It is, in particular, independent of the stress or strain fields within the region near the contact between grains

1 and 3. Denoting the grain diameter (or typical grain size) as a, contact regions, of typical (linear) size l, with $l \ll a$, may be dealt with as points. Interactions between a pair of contacting grains involve some surface force density over the contacting parts of their surfaces. The total force $\mathbf{F}$ and the total torque $\mathbf{\Gamma}$ should be obtained on integrating this density. If the torque is evaluated at the centre of the contact region, then $||\mathbf{\Gamma}||$ is of order $||\mathbf{F}||.l$, which may be neglected as the evaluation of global torques on grains involve terms of order $||\mathbf{F}||.a$. In most applications the local scale interaction law used in granular material modeling is a *contact law*, i.e. a relation between the motion of the pair of grains in contact and the *contact force*, regarded as a point force exerted on the surface of each grain.

One remarkable consequence of the scale separation between contact regions and grains is the validity of the *effective stress principle* (Mitchell and Soga, 2005), for fluid-saturated granular materials. Considering (Fig. 2)

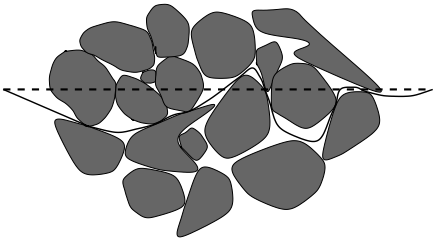

Figure 2. Two different surfaces through which stresses can be evaluated inside a saturated granular material, a flat one (dashed line) crossing through the grains, and another one (solid line), with hills and troughs, entirely comprised within pore space, except for very small contact regions.

a granular material with its pore space filled with a fluid at pressure P_l, the global stress tensor in such a medium, assumed homogeneous and in equilibrium, may be deduced from the force density transmitted through a fictitious cutting surface. As illustrated by Fig. 2, this surface may be placed entirely within the interstitial fluid-filled space, except for very small intergranular contact regions. The stress tensor, $\underline{\underline{\sigma}}$, may thus be written as a sum:

$$\underline{\underline{\sigma}} = \underline{\underline{\sigma}}^{\text{cont}} + P_f \underline{\underline{\mathbf{1}}}, \tag{1}$$

in which P_f is the fluid pressure and $\underline{\underline{\sigma}}^{\text{cont}}$ is the stress tensor associated with the contact forces (we adopt the soil mechanics convention, according to which compressive stresses are positive). As every grain is, in good approximation, entirely embedded within the fluid, the net force and torque

due to the fluid pressure, which is uniform at equilibrium, vanish. Consequently, neglecting the compression of the solid grains caused by the surrounding pressure, the granular system with its contact network is in the same situation as in the absence of interstitial fluid, with contact forces balanced on each grain corresponding to stress $\underline{\underline{\sigma}}^{\mathrm{cont}}$, as if this *effective stress* were applied to the dry material.

A counterexample of a system which should not, a priori, be dealt with as an ordinary granular material in the preceding sense, is illustrated in Fig. 3. Such objects with flat or conforming surfaces as shown in Fig. 3 may contact

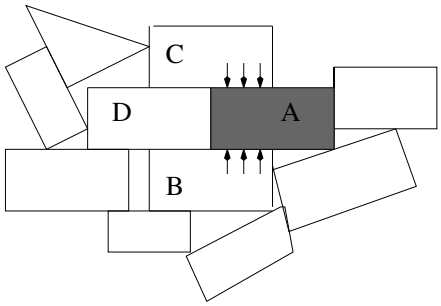

Figure 3. Brick-shaped grains may contact their neighbours through a notable part of their surface.

one another through a significant part of their periphery. Consequently the strains caused by contact stresses will extend through large domains inside the solid grains. Different contacts of the same grain may interfere with one another, as in the case (Fig. 3) of contact A-D, which should be affected, because of the Poisson effect, by the stresses in contacts A-B and B-C. Such systems should in principle require continuum mechanics boundary value problems to be dealt with in each solid grain, as opposed to granular systems in the sense of Fig. 1, for which the contact mechanics treatment of interactions usually regards each grain of a given pair as a (semi-infinite) half space. Obviously, the arguments used in connection with Fig. 2 justifying the effective stress principle in saturated granular materials do not necessarily apply in this case.

However, apparently conforming surfaces, or flat ones, enabling large contact areas, may not actually exist in the presence of smaller scale roughness, as sketched in Fig. 4. In such a case, the granular modelling approach may be salvaged, because the strain will tend to be confined to a thin region, of a thickness similar to the size of the asperities. Note also that the effective stress principle might apply, since the saturating liquid will invade

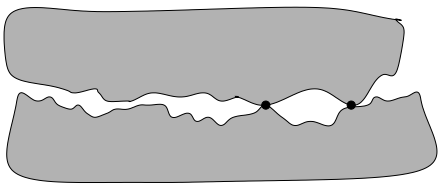

Figure 4. Schematic blown-up view of a contact between two nominally flat grain surfaces, showing their small scale roughness. Contact actually takes place via isolated points.

the interstitial region, save for the isolated asperities in contact. The practice of DEM modeling of polygonal grains (Azéma et al., 2012, 2013) may be justified thanks to this implicit assumption of roughness and contacts through isolated nearly punctual regions.

2.2 Contact laws

From the separation of scales and the resulting possibility of a formulation of granular mechanics with the discrete degrees of freedom associated with a collection of rigid objects, as discussed in Sec. 2.1, the *contact law* is an essential input of a granular model at the microscopic scale. In general, contact behaviors differs significantly from bulk material behaviors, being influenced by the fine details of the surface geometry– such a basic property as the intergranular friction angle is not a property of the material which the grains are made of.

Contact mechanics is a complicated field, because local problems to be dealt with in the contact region between two grains involve boundary conditions on an a priori unknown part of the surfaces, where both objects contact each other. The treatise by Johnson (1985) deals with many aspects of contact mechanics, but some difficulties related to surface roughness are hardly addressed. The presentation given here evokes the most consequential (for granular mechanics) features of contact mechanics and stresses the frequent use of simplified model, which hopefully contain the most important ingredients.

Fortunately, it is usually observed that the global, collective behavior of granular assemblies is not sensitively dependent on many features of the contact law. The relevance of contact models is often only evaluated *a posteriori*, on comparing numerical results to laboratory measurements on similar systems.

Friction. Coulomb friction is the most important mechanical property of intergranular contacts. While tribologists keep investigating realistic, complex, history-dependent models involving "third bodies" in the contact region (Richard et al., 2007), in the presence of a large number of grains and contacts as in a granular material sample, it is a common practice to stick to the simplest model for friction, the Coulomb model, with a constant friction coefficient μ in all contacts between similar bodies. The physical origin of friction is generally accepted to reside in the plasticity of small asperities through which the two bodies are contacting each other, because of their small scale roughness, despite the apparent smooth surfaces on the scale of the grain diameter or radius of curvature (Bowden and Tabor, 1950). As the stress in such asperities coincides then with the plastic threshold σ_c in normal indentation, the real contact area A_c has to increase proportionally to the total normal force $F_N = A_c\sigma_c$ transmitted in the contact region. The plastic shear resistance τ_c then yields the total tangential force F_T in sliding as $F_T = A_c\tau_c$, whence the Coulomb friction coefficient $\mu = \tau_c/\sigma_c$, independent of the normal load and of the apparent area of the contact. Many additional sophistications, involving aging and/or dynamic instabilities may affect the frictional behavior (Baumberger and Caroli, 2006), but the simplest friction as defined by

$$\begin{array}{ll} ||\mathbf{F}_T|| < \mu F_N & \text{no sliding} \\ ||\mathbf{F}_T|| = \mu F_N & \text{sliding,} \end{array} \tag{2}$$

is most often deemed sufficient to provide a satisfactory description of granular material behavior. Friction is said to be fully mobilized in the contact in the second case (equality).

Elasticity. The elastic response of a contact region is of course strongly dependent on its shape, and differs for sharp edges, pointed corners or smooth surfaces with a well-defined curvature. In the latter case, for grains made of an elastic material with Young modulus E and Poisson ratio ν the normal elastic force F_N in the contact relates to the normal deflection, h, by the Hertz law, which reads for spherical beads of diameter a:

$$F_N = \frac{\tilde{E}}{3} a^{1/2} h^{3/2}, \tag{3}$$

in which notation $\tilde{E} = E/(1-\nu^2)$ is adopted. The non-linearity stems from the growth with h of the contact region, a disk with radius b proportional to $\sqrt{ah}$. Johnson (1985) gives a detailed derivation of (3) and other contact laws, based on the assumption, adequate for small enough deflections, that

each contacting object might be locally dealt with as an infinite half space. Relation (3) is easily generalized (Johnson, 1985) to beads of different diameters (just use $a = \frac{2a_1a_2}{a_1+a_2}$ for diameters a_1, a_2), or to objects with two different (positive) radii of curvature. Note that exponent 3/2 may be obtained from a simple scaling argument: first, $b \propto \sqrt{ah}$ may be deduced from the contact geometry (the contact region radius being of the order of the "interpenetrated region" of non-deformed spherical balls); then a strain of order h/b is assumed to be distributed over a volume of order b^3, whence an elastic energy scaling as $Ea^{1/2}h^{5/2}$ and a force scaling as $Ea^{1/2}h^{3/2}$. Other contact shapes could result in different forms of normal elastic forces, e.g. scaling as h^2 for a sharp angular edge (Johnson, 1985). The Hertz law (3) does not apply for sands, but proves quite robust as model materials made of beads or smooth shapes are tested, for which elastic moduli might be measured (Jia et al., 1999; Kuwano and Jardine, 2002). Anticipating that elastic contact deflections play a minor role in granular material mechanics, contact elasticity is also often assumed linear in DEM calculations: a constant stiffness $K_N = \frac{dF_N}{dh}$ (possibly dependent on particle radii) is assumed to relate force and deflection as $F_N = K_N h$, instead of the Hertz law implying

$$K_N = \frac{\tilde{E}}{2} a^{1/2} h^{1/2} = \frac{3^{1/3}}{2} a^{1/3} \tilde{E}^{2/3} F_N^{1/3}. \tag{4}$$

Such a simplification is adopted with the assumption that a certain limit of rigid grains, in which contact deflections are irrelevant, is approached.

The normal law relating F_N and h should be supplemented by a tangential contact law relating the variations of the tangential component of the contact force, $\mathbf{F}_T$, to the variation of tangential relative displacements. The modeling of such laws is quite complicated, because of the interplay of elasticity and friction. Friction is modeled locally, as a condition similar to (2) applying to the force density, i.e. to stress vector $\mathbf{T} = \underline{\underline{\sigma}} \cdot \mathbf{n}$ within the contact surface, $\mathbf{n}$ denoting the normal unit vector. The situation of two spherical objects pressed against each other by a *constant* normal force F_N, the contact being subjected to a *varying* relative tangential displacement δU_T, as investigated by Mindlin and Deresiewicz (1953) reveals a history-dependent distribution of sliding regions within the contact surface. As δU_T increases from zero, sliding (relative tangential motion, where $||\mathbf{T}_T|| = \mu T_N$) takes place in an outer annulus of increasing width (Fig. 5), until all the contact may slide as the Coulomb equality applies everywhere to force density $\mathbf{T}$ and, consequently, to the global contact force. However, upon reversing the direction of the relative tangential motion, before this global sliding threshold is reached, a second annulus appears at the periphery of the contact region, within which sliding takes place in the opposite direction (Fig. 6).

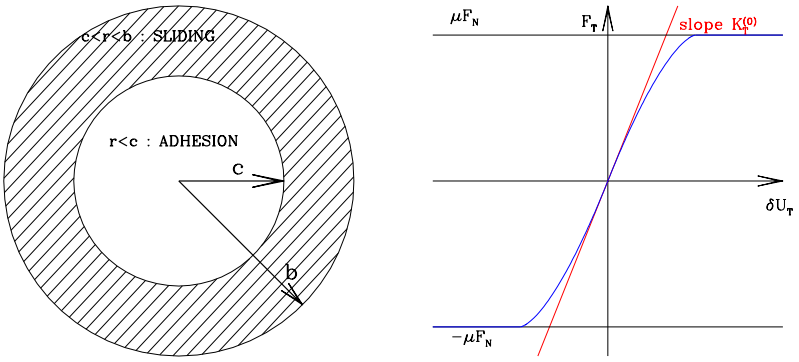

Figure 5. Left: initiation of a slip annulus at the periphery of the contact region as relative tangential displacement δU_T is imposed. Right: tangential force F_T versus δU_T.

Accurate modeling of contact elasticity in a granular sample with many

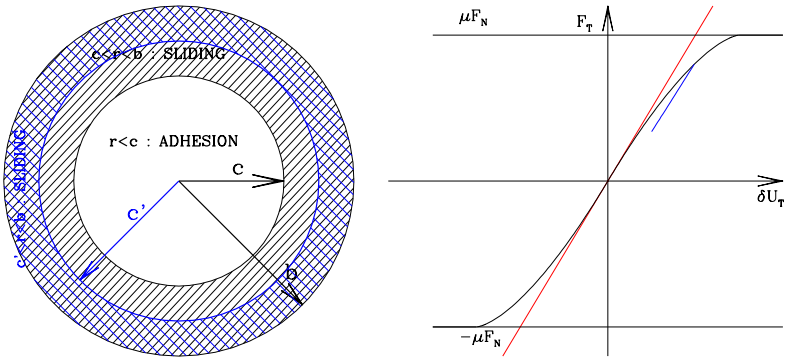

Figure 6. Left: appearance of a second slip annulus at the periphery as relative tangential displacement δU_T starts to decrease. Right: tangential force F_T versus δU_T (note beginning of unloading path)..

contacts thus seems to become almost hopelessly complicated, as records of all past changes in relative motion directions in the contacts should appar-

ently be kept. This is not, however, the whole story: one should be able to predict the variations of contact forces for arbitrary relative motions of contacting grains. Elata and Berryman (1996) pointed out that, even if the Coulomb threshold is reached nowhere in the contact (as in the hypothetical situation of an infinite friction coefficient μ) different stress and force density patterns in the contact region, and a different global tangential contact force F_T, may be obtained for the same values of deflection h and relative tangential displacement δU_T, depending on the past history of those variables. This is visualized in Fig. 7, reproduced from this paper. The results

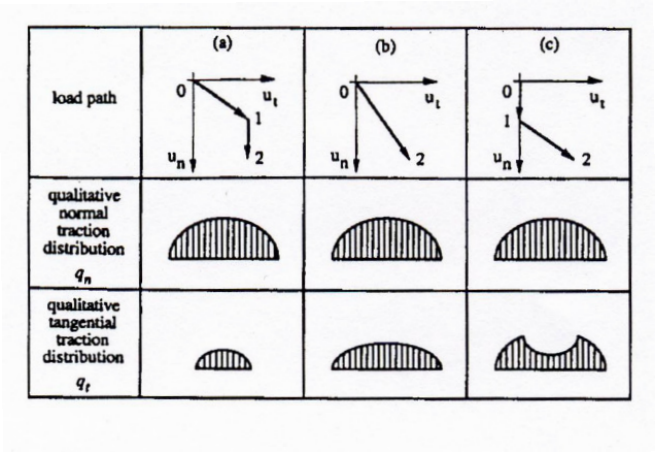

Figure 7. Different paths leading to the same final values of relative displacements (with notations u_n for h and u_t for δU_T), normal ($q_n = T_N$) and tangential ($q_t = T_T$) force densities across disk-shaped contact region.

of three different contact loading paths are shown, all ending at the same point in plane ($u_n = h, u_t = \delta U_T$): (a) increase u_n and u_t proportionally (1), along a straight line, so that u_t reaches its final value, but not yet for u_n, then increase only u_n (2) ; (b) increase both u_n and u_t proportionnally to their final values; (c) proceed as along path (a), but reversing the roles of u_n and u_t. Although the normal force density is the same, tangential force distributions are path-dependent. Elata and Berryman (1996) show this suprising conclusion to hold even in the absence of friction mobilization (i.e. in the limit of very large friction coefficient μ). Strictly speaking, the contact never behaves elastically, even in the absence of friction effects.

Facing such difficulties, a widely accepted approximation consists in

keeping a tangential stiffness $K_T = \dfrac{dF_T}{d(\delta U_T)}$ independent of δU_T, and coinciding with its value $K_T^{(0)}$ for $\delta U_T = 0$:

$$K_T = K_T^{(0)} = \frac{2-2\nu}{2-\nu} K_N = \alpha_T K_N = \frac{2-2\nu}{2-\nu} \frac{\tilde{E}}{2} a^{1/2} h^{1/2}, \tag{5}$$

for identical beads of diameter a – thus a function of deflection h or normal elastic force F_N. Specific caution should however be exercised, requesting a suitable rescaling of K_T when h decreases – as suggested by Elata and Berryman (1996).

General relative motion, objectivity issues. Furthermore, it should be specified how the contact force evolves as the pair of grains move with arbitrary combinations of translations and rotations while maintaining the contact. While there appears to be no exact general solution, based on the detailed treatment of the problem of the contact between moving objects, in the available literature, adopted solutions should abide by the objectivity principle (Kuhn and Chang, 2006), i.e., be such that if both contacting grains move as one non-deforming solid, then the contact force should follow this rigid body motion. Such a solution is described, e.g., by Agnolin and Roux (2007a).

Adhesion. All identical particles are attracted to one another by surface forces of different origins (Israelashvili, 1991; Maugis, 2000), among which van der Waals ones are the most universal type. Such attractive interactions introduce a characteristic force scale F_0 and a range, some length D_0 (on the nanometric scale for van der Waals interactions). This corresponds to some adhesion energy of order $F_0 D_0$. For ideal spherical particles of diameter a, F_0 is of order Γa, Γ denoting the interfacial energy of the grain surface. Comparing F_0 to other forces in a granular material (say, gravity, scaling as a^3 or applied pressure, resulting in contact forces scaling as a^2), it is usually observed that adhesive forces are quite negligible for grains sizes above the 10 μm range – this is the reason why cohesion effects are notable in fine powders, such as flour, or fine soils like silts, but not in sands. Furthermore, adhesive forces, given their extremely small range, are most frequently dominated by roughness effects, and turn out to be of order Γd, with $d \ll a$ corresponding to some asperity size (Castellanos, 2005). Exact calculations combining adhesive forces and Hertz elasticity are available – in the so-called Johnson-Kendall-Roberts (JKR) and Deriaguin-Muller-Toporov (DMT) cases (Maugis, 2000), corresponding to small or large values of the ratio (sometimes termed Tabor number, with definitions

varying by factors of order 1) of elastic deflection under force F_0 to range D_0. Interpolation schemes (Castellanos, 2005) are available in intermediate cases. In practice such ideal calculations do not quantitatively apply to experimental systems in which grains have irregular surfaces, and, in order to simulate large collections of grains, simplified models are adopted, introducing a force law with some maximum attraction F_0 and some range D_0.

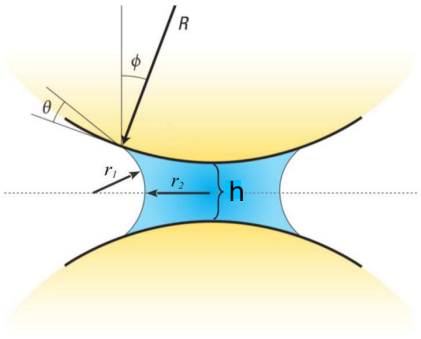

Figure 8. Liquid bridge joining two identical spherical beads.

One situation in which an accurate model might be used is that of wet grains, as liquid bridges form at contacts, or join pairs separated by a small distance, as sketched in Fig. 8. The contact law should then be replaced by an interaction law in which the grains are attracted to each other by a capillary force, which can be computed from Laplace's law (Lian et al., 1993; Pitois et al., 2000) (which states that the pressure within the liquid is lower than the external one, with difference $\gamma(\frac{1}{r_1} - \frac{1}{r_2})$, using the notations of Fig. 8, γ being the surface tension). Assuming simple rules might be identified to identify the spatial distribution of the liquid, such interactions can be dealt with in DEM (Radjaï and Richefeu, 2009; Khamseh et al., 2015). The maximum attractive force F_0 is observed for small bridge volumes (filling angle $\phi \ll 1$ on the figure), at contact ($h = 0$), is then, for wetting angle θ and bead radius $R = a/2$:

$$F_0 = 2\pi R\gamma \cos\theta. \tag{6}$$

In the presence of attractive forces, which act at a small distance, the Coulomb condition characterizing the contact surface behavior applies to the repulsive elastic component of the normal force. Fig. 9, from a DEM

study of a model system by Gilabert et al. (2007), displays the Coulomb cone within which the point of coordinates N_{ij}, T_{ij} (the normal and tangential force components in contact between grains i and j) should remain. N_{ij} is

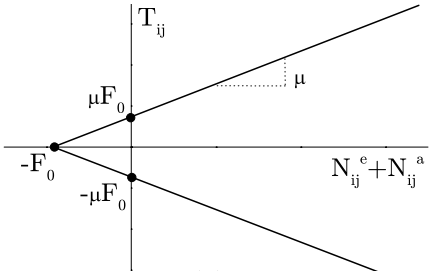

Figure 9. Coulomb condition in the presence of attractive force $-F_0$ in contact between grains i and j.

the sum of the adhesive contribution $N_{ij}^a = -F_0$ and the repulsive elastic one N_{ij}^e The tip is no longer at the origin of coordinates. The tangential force may reach intensities as large as μF_0 when the total tangential force vanishes because the elastic repulsion compensates attraction $-F_0$.

Resistance to rolling. It might be necessary in some cases to account for a finite lateral extension l of the contact region (yet small compared to diameter a), which causes a local torque $\mathbf{\Gamma}$. Physical motivations of existing models for *rolling and pivoting resistance* should involve surface asperities such that grain pairs interact through several contact points separated by distance l. A *rolling friction* coefficient, μ_R, and a *pivoting friction* coefficient μ_P are often introduced, such that inequalities analogous to (2) apply to normal and tangential components of $\mathbf{\Gamma}$, as follows.

$$\begin{aligned} |\Gamma_N| &\leq \mu_P F_N \qquad \text{(pivoting)} \\ ||\mathbf{\Gamma}_T|| &\leq \mu_R F_N \qquad \text{(rolling)}. \end{aligned} \tag{7}$$

By definition, both coefficients μ_R and μ_P hav the dimension of a length. They should be of order l. Below the threshold, torque components should vary more or less elastically with the relative rotation of both objects i and j, i.e., $\mathbf{n}_{ij}$ denoting the unit normal vector, for small rotation vectors $\vec{\omega}_i$ and $\vec{\omega}_j$, Γ_N relates to the pivoting angle, $\mathbf{n}_{ij} \cdot (\vec{\omega}_i - \vec{\omega}_j)$, while $\mathbf{\Gamma}_T$ is linked to the rolling motion, involving the tangential component $(\underline{\underline{\mathbf{1}}} - \mathbf{n}_{ij} \otimes \mathbf{n}_{ij}) \cdot (\vec{\omega}_i - \vec{\omega}_j)$. This model of rolling and pivoting friction is thus analogous to the classical model of sliding friction.

The implementation of rolling resistance with spherical or circular grains can be deemed analogous to the modeling of non-spherical shapes, especially angular ones, for which contacts may extend to parts of faces or edges on the grain periphery. Such a correspondance has been proposed in quantitative form for two-dimensional grains by Estrada et al. (2011).

In the presence of adhesive forces, analogously to the Coulomb condition for the tangential force, inequalities (7) apply with the sole elastic repulsive component of normal force F_N in the right-hand side. Thus, in contacts

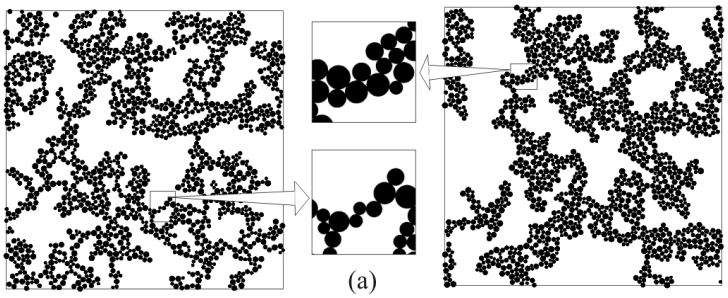

Figure 10. Aspect of cohesive grain clusters in a simple 2D model, with (left) and without (right) rolling friction. Blown-up details (a) show elongated parts joining denser regions (Gilabert et al., 2007).

where the total normal force vanishes, a finite torque $\mu_R F_0$ ($-F_0$ denoting the adhesive force as before), or $\mu_P F_0$ in the normal direction, might be transmitted. This has important consequences on the possible morphologies of assemblies of adhesive grains, as illustrated in Fig. 10, from Gilabert et al. (2007). These disk-shapes grains are assembled here under small external stress, and form rigid structures in equilibrium. Some resistance to rolling is necessary for the single particle strands to remain stable and rigidly transmit forces. In the absence of rolling friction, thin "arms" (rigid elongated structures) are made of at least two grains in the transverse direction.

Viscoelastic or plastic dissipation in collisions. In addition to elastic and frictional forces (and, possibly, to adhesive ones), grains in contact exert onto one another viscous, dissipative force depending on their relative velocity. Typically, one writes normal and tangential forces proportional to

corresponding relative velocities, and opposing the relative motion:

$$\begin{aligned} F_N^v &= \alpha_N \frac{dh}{dt} \\ \mathbf{F}_T^v &= \alpha_T \frac{d(\delta U_T)}{dt}, \end{aligned} \tag{8}$$

with damping coefficients α_N, α_T, possibly dependent on relative displacements h, δU_T (or the elastic part of the latter). One physical origin of such viscous forces is the viscoelasticity of the grains (Ramirez et al., 1999; Brilliantov and Pöschel, 2004), which always exists on small time scales. In practice, the choice of a damping model seldom relies on a true physical analysis of the microscopic origins of viscous dissipation. Damping coefficients are related to coefficients of restitution in binary collisions (Maw et al., 1976), which in general (and in particular in the case of viscoelastic effects in Hertzian contacts) depend on the initial relative velocity. The normal coefficient of restitution, e_N is defined by the ratio, equal to $-e_N$, of the receding relative velocity in the normal direction after the collision to the approaching relative velocity in the normal direction before the collision. Its counterpart e_T is defined analogously with tangential relative velocities. In the simplest case of linear unilateral elasticity, without adhesive forces, a constant coefficient α_N corresponds to a constant normal coefficient of restitution e_N, which is readily obtained on solving for the motion of a damped linear oscillator. For a pair of identical beads of mass m, the "critical" value of α_N, separating the oscillating from the overdamped regimes is $\alpha_N^c = \sqrt{2mK_N}$ and e_N depends on ratio $\zeta = \alpha_N/\alpha_N^c$, assumed below 1, as

$$e_N = \exp\left[\frac{\pi\zeta}{2\sqrt{1-\zeta^2}}\right]. \tag{9}$$

With Hertzian contact elasticity, viscous damping may be chosen in reference to the critical damping of a linear contact with stiffness K_N equal to the instantaneous deflection-dependent value. Such a choice results in a velocity-independent coefficient of restitution.

2.3 Collective behavior and contact behavior

The contact behavior may be represented as a combination of rheological elements, as shown in Fig. 11, (for a contact without adhesive forces, no resistance to rolling or pivoting, and no viscous force in the tangential direction). In an upscaling procedure, leading to macroscopic behavior, the characteristics of those elements, as well as the geometry of the grains and the contact network, are the microscopic inputs. We now recall some basic

Figure 11. Rheological elements schematizing contact behavior: normal force (left) combines a spring (possibly nonlinear, with K_N depending on elongation), a viscous dashpot, and a no-tension joint (no adhesion here). The tangential law (right) involves a plastic slider.

aspects of macroscopic granular mechanics and confront them to microscopic features, to get some insights on the feasability of such an upscaling procedure and the relative importance of the different inputs.

Classical quasistatic stress-strain behavior: triaxial compression. The quasistatic stress-strain behavior of cohesionless granular materials is commonly measured in tests as triaxial compression, as schematized in Fig. 12. Starting from an equilibrated pack under isotropic stresses, one principal stress, σ_1 gradually increases, along with the conjugate strain ϵ_1, while the lateral stresses, and thus the other two principal stresses, $\sigma_2 = \sigma_3$, are maintained fixed. Results are traditionally expressed in terms of deviator stress $q = \sigma_1 - \sigma_3$ and volumetric strain $\epsilon_v = 1-(1-\epsilon_1)(1-\epsilon_3)(1-\epsilon_3)$ plotted versus *axial strain* $\epsilon_a = \epsilon_1$. These curves differ according to the solid fraction Φ in the initial isotropically loaded state. q steadily increases to an asymptotic value q_c at large axial strain in the loose case, while it first passes through a maximum (the "deviator peak") in the dense case, before decreasing to the same large strain plateau value q_c, in initially dense systems. Meanwhile, loose systems contract, and dense systems, after some initial contraction, dilate, until some asymptotic value Φ_c of solid fraction is approached, which turns out to be the same whatever the initial density. A loose initial state is therefore defined by $\Phi < \Phi_c$, a dense one by $\Phi > \Phi_c$. This large strain state reached after the material has been monotonically deformed in the same direction is known as the *critical state* (Wood, 1990) – we shall return, in Sections 5 and 6, to the important role of the critical state in granular material rheology.

The maximum value of q (either at the peak or at the final plateau) is

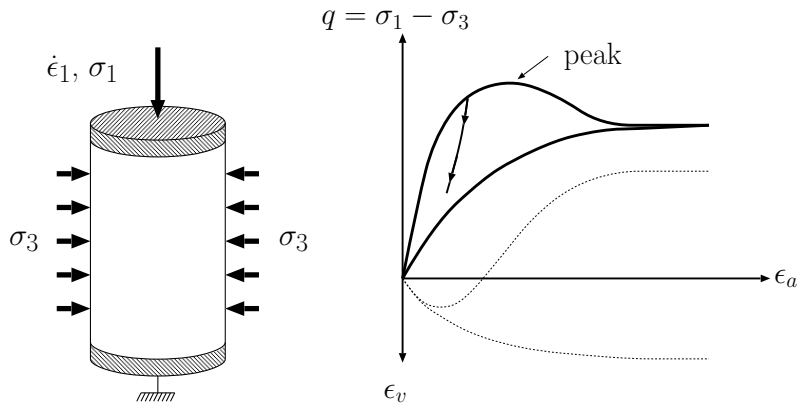

Figure 12. Left: schematic view of an axisymmetric triaxial compression test. Right: typical results in dense and loose systems. Deviator stress q (solid lines) and volumetric strain ϵ_v (dotted lines) versus axial strain ϵ_1. Note the deviator peak in the dense case.

associated to the internal friction coefficient φ of the material as:

$$\frac{q}{\sigma_3} = \frac{2\sin\varphi}{1-\sin\varphi}. \tag{10}$$

A familiar notion, the internal friction angle should coincide with the maximum slope angle of a free surface of the material under gravity or angle of repose (Nedderman, 1992), provided the plastic failure associated with the deviator peak (dense case) or the critical plateau (loose case) satisfies the Coulomb criterion – the yield criterion given as a function of principal stresses $\sigma_1 \geq \sigma_2 \geq \sigma_3 \geq 0$ by

$$f(\underline{\underline{\sigma}}) = \frac{\sigma_1 - \sigma_3}{2} - \frac{\sigma_1 + \sigma_3}{2}\sin\varphi \leq 0 \tag{11}$$

In practice, the yield properties of simple materials, such as sands or assemblies of spherical beads (Suiker and Fleck, 2004; Peyneau and Roux, 2008b), are better described by other forms of the yield criterion (Lade and Duncan, 1975), and the apparent value of φ as identified from (10) might be slightly different from the one applicable to a shear test (which is more directly the angle of repose).

(Over)simplified laws, similarity with contact behavior. For simplicity (e.g., in engineering practice, for lack of very detailed information on

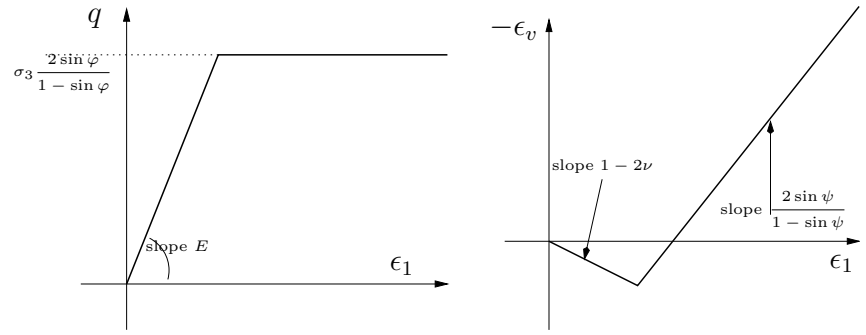

Figure 13. Simplified elastoplastic law for triaxial compression: deviator stress (left) and volumetric strain (right) versus axial strain.

a certain granular soil) the behavior as measured in a triaxial compression test of a cohesionless dense granular material might be described as shown in Fig. 13, assuming linear isotropic elasticity to apply up to the deviator peak, with a macroscopic Young modulus E and Poisson ratio ν, and then a constant slope (or *dilatancy*) $-\frac{d\varepsilon_v}{d\varepsilon_a}$, as the maximum deviator (confused here with the final plateau) is reached.

This is of course quite a gross simplification, unlikely to accurately describe a situation in which the softening after the peak (shown in Fig. 12, ignored in the simplified version of Fig. 13) plays an important role. Furthermore, the prepeak behavior is not elastic (as indicated in the sketch of an unloading curve in Fig. 12).

But, at first sight, the first graph of Fig. 13 is quite similar to the simplified version of the tangential contact law of Fig. 5, in which the slope is taken constant (equal to $K_T^{(0)}$ in Eq. 5) and variations are assumed elastic before the Coulomb threshold μF_N is reached. Both describe similar elastoplastic behaviors, and the analogy is strengthened by the use of a common vocabulary ("Coulomb threshold", "friction"...). Should one regard the increase of q with ε_a as a macroscopic consequence of the contact behavior and internal friction as a reflection of intergranular friction? As shown below, such a naïve view is however misleading.

Dilatancy. One qualitative difference between microscopic and macroscopic behaviors is the existence of macroscopic dilatancy (or contractancy for loose systems). Dilatancy may be described as a flow rule, which for the volumetric strain behavior shown in Fig. 13 is associated with plastic po-

tential $g(\underline{\underline{\sigma}})$ written below (i.e., the plastic strains are given by $\underline{\underline{\varepsilon}}^P = \lambda \frac{\partial g(\underline{\underline{\sigma}})}{\partial \underline{\underline{\sigma}}}$ with $\lambda > 0$):

$$g(\underline{\underline{\sigma}}) = \frac{\sigma_1 - \sigma_3}{2} - \frac{\sigma_1 + \sigma_3}{2} \sin \psi, \tag{12}$$

where a dilatancy angle, ψ, is introduced.

After Reynolds (1885), who coined the word "dilatancy", this property is usually interpreted as the result of deformation mechanisms on the scale of local grain arrangements (Goddard and Didwania, 1998), in which grains or rows of grains slide onto one another, as depicted in an elementary 2D example in Fig. 14. Although rather simplistic, such an approach stresses

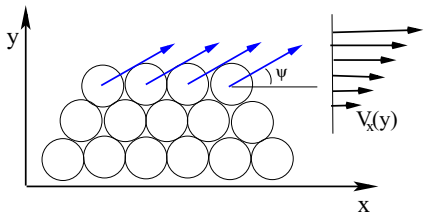

Figure 14. A simple example of alleged mechanism for dilatancy with 2D rows of disks sliding past one another in shear flow.

the collective origins of dilatancy, as an effect of steric hindrance in relative grain motion. It will be questioned below in Sec. 5.

Granular disorder: forces and displacements. Attempts at averaging the local behavior to obtain macroscopic laws are confronted with the characteristic disorder of granular materials. As shown in Fig. 15, force patterns comprise typical alignments of strongly loaded contacts (the *force chains*), while some regions (involving 5 to 10 grains in this case) carry little stress. Some grains (the *rattlers*) are not involved in the force-carrying contact network and are left free to move in the "cage" formed by their load-carrying neighbours. Many studies have been devoted to the statistical distribution of force values (Coppersmith et al., 1996; Radjaï, 2015). The probability distribution function often decreases exponentially for large values, but forces, say, 4 times as large as the average represent a small, but notable fraction of the total number (say, of order 10^{-3}). The role and the persistence of the stronger force chains, carrying stress anisotropy, while smaller forces prevent them from buckling, was also discussed (Radjaï et al., 1998). As to displacements, Fig. 16 evidences equally disordered patterns (Kuhn, 1999; Roux and Combe, 2002; Radjaï and Roux, 2002), involving many

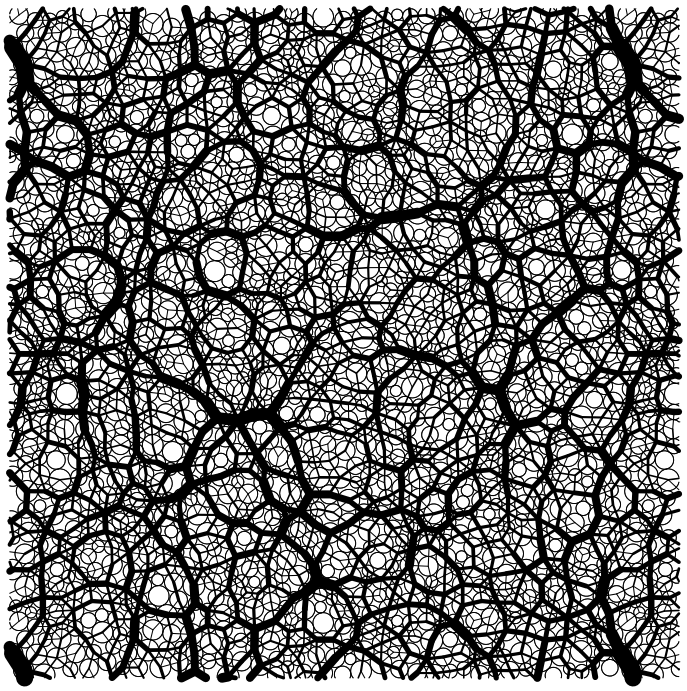

Figure 15. Equilibrium contact forces, balancing externally applied isotropic pressure, in 2D sample of disks. Stroke thickness is proportional to normal force intensity.

vortex structures of large scale, comparable to the sample size. The figure actually shows the "non-affine part" of the displacements, i.e., for each grain i, the displacement $\mathbf{u}_i$ of its centre, positioned in $\mathbf{r}_i$, minus its value in a homogeneous continuum subjected to the same (small) strain $\underline{\underline{\epsilon}}$, i.e., for a certain choice of the origin and in the absence of macroscopic rotation (the sign being due to our convention that strains are positive for shrinking lengths):

$$\tilde{\mathbf{u}_i} = \mathbf{u}_i + \underline{\underline{\epsilon}} \cdot \mathbf{r}_i. \tag{13}$$

Fig. 16 corresponds to ε_1, ε_2 of order 10^{-3}, while $\epsilon_{12} = 0$. The importance of non-affine displacements might be assessed on evaluating, in a sample of

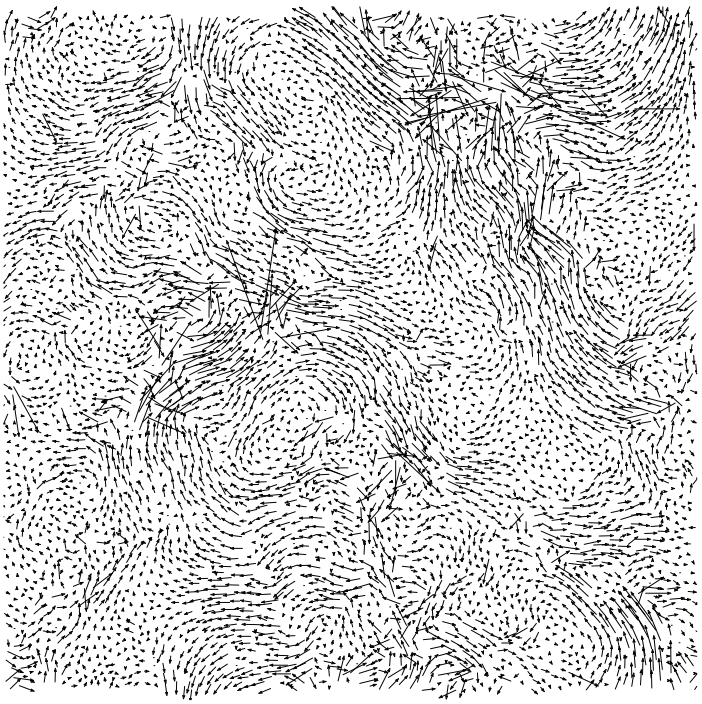

Figure 16. Non-affine part of grain displacements (arbitrary scale) corresponding to strain interval 10^{-3} in 2D disk assembly in biaxial compression.

N grains of average diameter a the following ratio:

$$\Delta = \frac{1}{Na^2||\underline{\underline{\epsilon}}||^2} \sum_{i=1}^{N} ||\tilde{\mathbf{u}}_i||^2. \tag{14}$$

Values of Δ of order 10 or 100 are quite common.

The role of geometric rearrangements of contact networks. Since the contact laws rule the mechanical properties at the grain scale, it may be tempting to expect that the macroscopic behavior could be retrieved on suitably averaging the contact behavior, as in homogenization approaches to the macroscopic properties of microscopically heterogeneous materials (Nemat-Nasser and Hori, 1993). Can one regard the granular sample as a network of rheological elements as shown in Fig. 11? The following simple example (Roux, 2000) shows that the deformation corresponding to certain

changes in the applied load may not result from contact mechanics averaged on a larger scale. Consider the set of four rigid frictionless disks shown

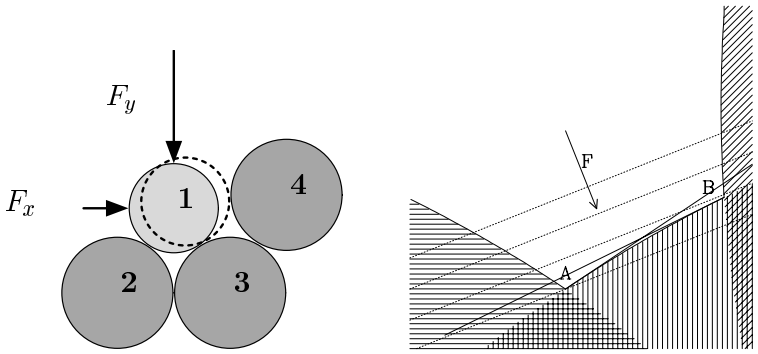

Figure 17. Left: simple model system. One mobile disk (1) , in contact with fixed ones (2, 3 and 4), and subjected to external force with components F_x, F_y. All disks are rigid and frictionless. Two possible equilibrium positions: light grey disk, dashed contour. Right: equipotentials (dotted lines) and regions of plane forbidden to centre of disk 1 by steric exclusion (hashed zones). A and B mark equilibrium positions with two contacts.

in Fig. 17 (left graph), with only one mobile grain (disk 1), subjected to an external force. Depending on the orientation of **F**, disk 1 might find an equilibrium position (grey disk) with contacts with disks 2 and 3, or another one in contact with 3 and 4 (disk outlined with dashed perimeter). With no friction and no contact elasticity, the potential energy $W = -F_x.x - F_y.y$, constant on lines orthogonal to vector **F**, is to be minimized at equilibrium, under the constraint that disks do not overlap.These are the two possible equilibrium positions marked A and B (right graph). As the direction of **F** gradually changes, the disk will move from one equilibrium position to the other, as soon as the steric exclusion constraints enable a motion with decreasing W. The concavity of the boundary of the accessible region for coordinates x, y (the intersection of the exterior parts of circles) entails that the relation between $Q = F_x/F_y$ and the equilibrium position x of mobile disk 1 takes the form shown in Fig. 18. Position x change from x_A to x_B by sudden jumps, and corresponding values of Q are associated with destabilizations of equilibrium points A and B, as the equipotential line in the second graph of Fig. 18 becomes tangent to the excluded region (hashed zone).

One thus obtains a hysteretic relation, analogous to some effective fric-

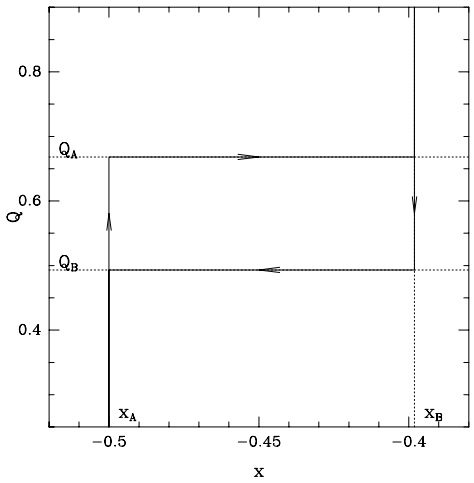

Figure 18. Hysteretic variations of equilibrium position x of mobile disk 1 of Fig. 17 (with possible values x_A and x_B corresponding to points A and B) with force parameter $Q = F_x/F_y$.

tion law, between x – an analog of strain – and Q – an analog of stress ratio. But the "strain" is entirely geometric, corresponding to a change in the contact list, and has no relation to the contact law (here reduced to its bare minimum: the grains cannot interpenetrate).

It should thus be expected that the macroscopic features of granular material mechanics stem from the geometry of granular packings and of their rearranging contact networks, as much as from contact laws.

3 Collective properties of granular assemblies

We now introduce important tools for the description of granular materials from a micromechanical point of view.

3.1 State variables

Solid fraction. The first variable characterizing the state of a granular material is its density or the *solid fraction*, Φ defined as the ratio of the volume of the grains to the volume occupied by the material sample (geotechnical practice tends to favour the *void ratio*, defined as $e = -1 + 1/\Phi$). Everyday experience with sand, ground coffee or potatoes shows that, as already recalled in connection with the behavior under deviatoric load (see

Fig. 12), solid objects can be assembled in stable, solidlike packs with different solid fractions. Identical disks in 2D achieve their densest arrangement if their centres are placed on the sites of a regular triangular lattice with spacing equal to their diameter, reaching area fraction $\Phi = \pi/(2\sqrt{3}) \simeq 0.91$. The densest possible structure of identical (3D) spherical balls are obtained on stacking such 2D lattices on top of one another, as shown in Fig. 19. Such a dense stacking should alternate between 3 possible horizontal place-

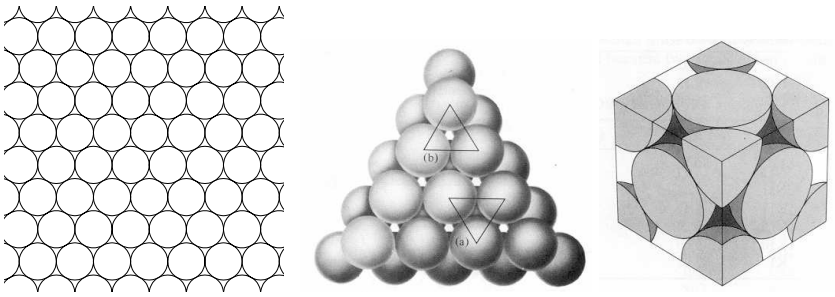

Figure 19. Regular lattices achieving maximum solid fraction. Left: triangular lattice for disks. Middle: building 3D maximum density lattices for beads on stacking such layers. Right: fcc lattice.

ments, and may result in the face-centered cubic lattice (fcc), the hexagonal compact one, or hybrids thereof. The achieved solid fraction in all cases is $\Phi = \pi/(3\sqrt{2}) \simeq 0.74$. Although such lattice structures are important in solid-state physics (Ashcroft et al., 2016) and the search for maximum density structures is a time-honoured endeavour for which mathematical proofs were only recently obtained (Aste and Weaire, 2000; Szpiro, 2003), they are certainly not representative of the generic disorder in granular materials.

More relevant (see Fig. 20) is the classical concept of *random close packing* (RCP), referring to a disordered state of maximum solid fraction Φ^* with no ordering, no "germ" of incipient crystallisation. The corresponding solid fraction, as observed both in experiments and simulations, is $\Phi^* \simeq 0.64$ for spherical balls. The absence of crystalline nuclei can be checked with suitable order parameters (Volkov et al., 2002; Agnolin and Roux, 2007a). 2D assemblies of monodisperse disks crystallize very easily, and thus should be avoided as a model material. 3D packs of equal-sized beads, on the other hand, are easily maintained in disordered states. DEM studies have revisited the RCP, which may be defined (Agnolin and Roux, 2007a) as an equilibrium state of rigid frictionless grains under isotropic pressure. Such states in which confining force are balanced by steric repulsion between

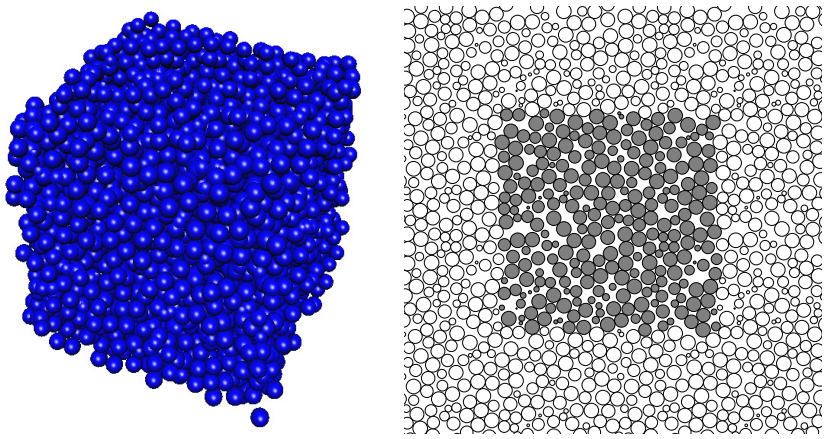

Figure 20. Spherical balls in RCP state: aspect of cubic sample (left), cut parallel to a face (right). Grey particles are within the periodic cell used in simulations.

hard objects are often referred to as *jammed states* in the recent physics literature (O'Hern et al., 2003; Somfai et al., 2007). Minimizing the potential energy of an applied isotropic pressure amounts to maximizing density, and normal contact forces play the role of Lagrange multipliers corresponding to impenetrability constraints. Compacting procedures thus appear as strategies to avoid the effects of friction. Some studies have shown that the RCP state is not unique – some larger densities might be obtained, even in systems that cannot crystallize because of the diameter distribution (Chaudhuri et al., 2010). RCP states, though, may still be defined as the disordered "jammed states" forming in the limit of fast assembling procedures. By construction, such states are local solid fraction maxima in configuration space. Fastly assembled ones turn out to be statistically similar and share the same solid fraction.

Coordination numbers. The coordination number, z, is defined as the average number of force-carrying contacts per grain. Thus, if N_c is the number of contacts and N the number of grains, one has $z = 2N_c/N$. As visible in Fig. 15, a proportion x_0 of "rattlers" carry no force.x_0 is about 1.5% in frictionless RCP states, and tends to vary with the friction coefficient. For μ of order 0.1-0.5, it may reach 10 to 15% in equilibrated frictional monosized sphere packs under uniform stress. Excluding those

rattlers from the averaging of contact numbers, one may define a corrected coordination number for the force-carrying structure (sometimes called the *backbone*):

$$z^* = \frac{z}{1 - x_0}. \tag{15}$$

The coordination numbers of the lattices of Fig. 19, $z = 6$ for disks and $z = 12$ for spheres, are unrealistically high compared to generically disordered granular materials, for which, as shown in Sec. 3.3 below, z^* is bounded for rigid, undeformable grains, to much lower values. Thus $z^* = 6$, obtained with rigid frictionless beads, is an upper bound in the presence of friction. As may be inferred from Fig. 20, a measurement of coordination numbers is difficult, even with sophisticated tomography techniques (Aste et al., 2005). Furthermore, the increase of pair correlation functions near contact (O'Hern et al., 2003; Somfai et al., 2007; Agnolin and Roux, 2007a) enhances the difficulty to distinguish really contacting pairs.

Fabric and force anisotropy. The contact network will influence the material behavior by its density (number of contacts per unit volume), conveniently expressed as

$$\overline{n}_c = \frac{z\Phi}{2v_1}, \tag{16}$$

in which v_1 denotes the average grain volume. It is also characterized by the statistics of contact orientations, as expressed by the distribution $\mathcal{P}(\mathbf{n})$ of normal unit vectors on the unit sphere Σ, such that $\int_\Sigma \mathcal{P}(\mathbf{n}) d^2\mathbf{n} = 1$, and $\mathcal{P}(-\mathbf{n}) = \mathcal{P}(\mathbf{n})$ since $\mathbf{n}$ and $-\mathbf{n}$ play the same role. $\mathcal{P}(\mathbf{n})$ may be expressed with spherical coordinates θ, φ and expanded on the basis of spherical harmonics. $\mathcal{P}(\theta, \varphi)$, its density with respect to the uniform measure $\frac{1}{4\pi} \sin\theta \, d\theta \, d\varphi$, reduces to a function of θ for axisymmetric states (no dependence on φ), which is in fact an even function of $\cos\theta$, expressible as a linear combination of Legendre polynomials of even order, as follows:

$$\begin{aligned} p(\cos\theta) &= 1 + b_2 \frac{3\cos^2\theta - 1}{2} + b_4 \frac{35\cos^4\theta - 30\cos^2\theta + 3}{8} + \dots, \quad \text{with} \\ b_2 &= \frac{15}{4}\left[\langle\cos^2\theta\rangle - \frac{1}{3}\right]; \\ b_4 &= \frac{9}{16}\left\{35\left[\langle\cos^4\theta\rangle - \frac{1}{5}\right] - 30\left[\langle\cos^2\theta\rangle - \frac{1}{3}\right]\right\}; \\ &\dots\dots \end{aligned} \tag{17}$$

Such forms are adequate in systems assembled under gravity and/or subject to an axisymmetric compression process (e.g., triaxial, Fig. 12). Isotropic

systems are such that $|\cos\theta|$ is uniformly distributed between 0 and 1, whence $\langle\cos^{2k}\theta\rangle = 1/(2k+1)$ for any $k \geq 1$, and all coefficients b_{2k} in (17) vanish. The few first terms are often sufficient for a good representation

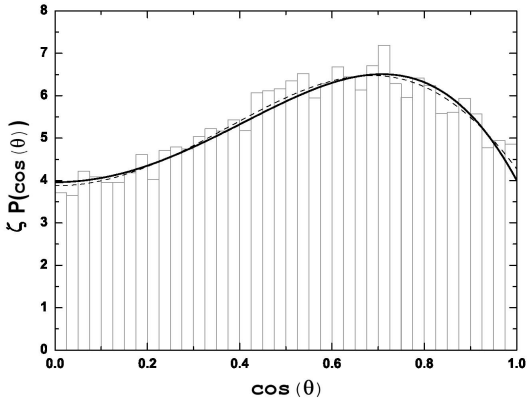

Figure 21. $\zeta P(|\cos\theta|)$ (coordination number $\zeta \simeq 5.2$ in this case) versus $|\cos\theta|$ in bead sample assembled under gravity. Histogram: numerical data. Expansion (17) to order 4 (solid line), and to order 6 (dotted line).

of contact orientation distributions, as evidenced in Fig. 21: probability distribution function $P(|\cos\theta|)$ (twice $p(\cos\theta)$ of Eq. 17 because of normalization) is well described by the expansion to order 4 (i.e., truncated after the terms explicitly written in Eq. 17).

The average normal force among all contact being denoted as $\langle F_N\rangle$, it is often useful to know how forces differ according to contact orientations. One thus defines $\mathcal{F}^N(\mathbf{n})$ as the average normal force carried by the contacts with normal direction $\mathbf{n}$, normalized by $\langle F_N\rangle$ (such that $\mathcal{F}^N(\mathbf{n})$ is uniformly equal to 1 in isotropic systems under isotropic pressure). $\mathcal{F}^N(\mathbf{n})$ may then be expanded in spherical harmonics or in Legendre polynomials in the axisymmetric case, just like $\mathcal{P}(\mathbf{n})$.

3.2 Contact forces and macroscopic stress.

Consider a granular sample, of volume Ω, made of grains labelled with indices i, $1 \leq i \leq N$, with masses m_i and velocities $\mathbf{v}_i$. Let us define $\mathbf{F}_{ij}$ the contact force, exterted by grain i onto its contacting neighbour j, and the *branch vector* $\mathbf{r}_{ij}$, pointing from the centre of i to the centre of j. Then if the system is subjected to a uniform stress $\underline{\underline{\sigma}}$, one has the following relation, in which α, β are indices of coordinates, and the second sum runs over all

contacts:

$$\sigma_{\alpha\beta} = \frac{1}{\Omega}\left[\sum_{i=1}^{N} m_i v_i^\alpha v_j^\beta + \sum_{i<j} F_{ij}^\alpha r_{ij}^\beta\right]. \tag{18}$$

This formula may be proved in various ways (Christoffersen et al., 1981; Iwashita and Oda, 1999), e.g., averaging the stress field within the grains, or dealing with the momentum transmission through cutting surfaces inside the sample. The first term of (18) vanishes in equilibrium (evaluating velocities in the frame of the centre of mass). One may then write

$$\sigma_{\alpha\beta} = \overline{n}_c \langle F_{ij}^\alpha r_{ij}^\beta \rangle, \tag{19}$$

from which, using (16), a simple, convenient relation may be extracted for spherical grains of diameter a, between the average stress $P = \mathrm{tr}\underline{\underline{\sigma}}/3$ and the average normal force:

$$P = \frac{z\Phi}{\pi a^2}\langle F_N \rangle. \tag{20}$$

This formula gives a quantitative form to the estimation of an order of magnitude of typical contact forces as $a^2 P$.

Denoting as $\underline{\underline{\sigma}}^N$ the contribution of normal force components to the stress tensor, and assuming, in an equilibrated assembly of spherical grains, that the average branch vector length is equal to the average diameter a, and uncorrelated to the contact force, one has

$$\sigma_{\alpha\beta}^N = a\overline{n}_c \langle F_N \rangle \int_\Sigma \mathcal{F}^N(\mathbf{n}) \mathcal{P}(\mathbf{n}) n_\alpha n_\beta d^2\mathbf{n} \tag{21}$$

In axisymmetric systems like those assembled under gravity and subjected to triaxial compression in the vertical direction, one may also define $\mathcal{F}^T$ as the force density, normalized by $\langle F_N \rangle$, in the tangential direction contained in the azimuthal plane – along vector $\mathbf{t}$ with non-negative coordinate along the axial direction from which angle θ is measured. In such cases, choosing this axis as axis of coordinate, one has for all diagonal components

$$\sigma_{\alpha\alpha} = a\overline{n}_c \langle F_N \rangle \int_\Sigma \mathcal{P}(\mathbf{n}) \left[\mathcal{F}^N(\mathbf{n}) n_\alpha n_\alpha + \mathcal{F}^T(\mathbf{n}) t_\alpha n_\alpha\right] d^2\mathbf{n}. \tag{22}$$

Then, useful approximation formulae are obtained on keeping the dominant anisotropic terms in expansions of $\mathcal{P}$ (defining coefficient b_2 as in expansion 17), of $\mathcal{F}^N$ (defining, analogously, coefficient b_2^N), and $\mathcal{F}^T$. In this latter case, one should pay attention to the different symmetry and write:

$$\mathcal{F}^T(\mathbf{n}) = b^T \sin\theta\cos\theta. \tag{23}$$

Keeping only the dominant anisotropic terms in the integral and neglecting their products, convenient fomulae are obtained (Azéma et al., 2009, 2013), which often prove quite accurate, expressing axial, σ_1, and lateral, σ_3, stresses as

$$\begin{aligned} \sigma_1 &= a\overline{n}_c\langle F_N\rangle \left[\frac{1}{3} + \frac{2}{15}\left(b_2 + b_2^N + b^T\right)\right] \\ \sigma_3 &= a\overline{n}_c\langle F_N\rangle \left[\frac{1}{3} - \frac{1}{15}\left(b_2 + b_2^N + b^T\right)\right]. \end{aligned} \tag{24}$$

Similar formulae may be derived in systems under shear tests (Peyneau and Roux, 2008b; Azéma and Radjaï, 2014), and, for grains of arbitrary shapes and polydispersities, the anisotropy of branch vectors might be accounted for (Azéma et al., 2009, 2013).

3.3 Contact networks and rigidity matrices

Definitions. The *rigidity matrix* is a central object in the relation between grain kinematics, contact behavior, and global properties of contact networks. It should not be confused with the *stiffness matrix*, expressing elastic or elastoplastic behavior. The rigidity matrix is a geometric object – its name originates in the theory of rigidity of structures assembled with cables, bars and joints (Thorpe and Duxbury, 1998). For a pair of grains i,

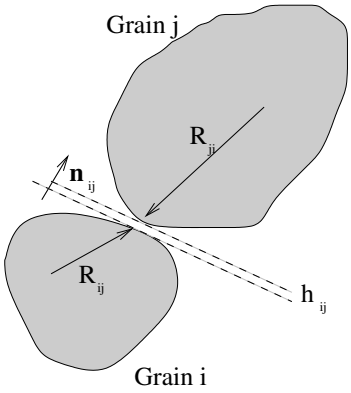

Figure 22. A pair of grains nearly in contact.

j in contact or very nearly in contact (separated by a very small distance h_{ij}), as represented in Fig. 22, one defines the corresponding semi-branch vectors $\mathbf{R}_i^j$, pointing from the (arbitrarily chosen) centre of i to the con-

tact point or the nearest point to the surface of j, and, similarly, $\mathbf{R}_j^i$, and the unit vector $\mathbf{n}_{ij}$ normal to the contact plane (or the incipient one). We choose one of the grains, say i, as the first object. Then, the contact laws of Sec. 2.2 involve the *relative displacement* of the contact point, i.e., the difference in displacements, δU_{ij}, according to the (rigid body) motions of the first and the second object. Denoting as $\mathbf{u}_i$, $\mathbf{u}_j$, the displaements of grain centres and $\vec{\omega}_i$, $\vec{\omega}_j$ their small rotations (displacements are actually assumed infinitesimal, like velocities), one has

$$\delta U_{ij} = \mathbf{u}_i + \vec{\omega}_i \times \mathbf{R}_i^j - (\mathbf{u}_j + \vec{\omega}_j \times \mathbf{R}_j^i). \tag{25}$$

Contact laws are more conveniently implemented on distinguishing the normal (scalar $\delta U_{ij}^N = \mathbf{n}_{ij} \cdot \delta U_{ij}$) and tangential (vector $\delta U_{ij}^T \perp \mathbf{n}_{ij}$) components of relative displacements. If the contact law admits rolling and pivoting torques, then (25) should be supplemented by the definition of relative rotation vector $\vec{\omega}_i - \vec{\omega}_j$. Assembling all degrees of freedom, one gets an N_f-dimensional vector, $\mathbf{U}$, whose coordinates comprise all those of displacements and rotations of the N grains. Depending on specific boundary conditions, involving walls, fixed objects, periodicity conditions... N_f might slightly differ from $ND(D+1)/2$ in dimension D (3 or 2). Likewise, let us define, with N_c contacts, an DN_c-dimensional vector $\mathcal{U}$ containing all normal and tangential components of relative displacements δU_{ij} in the contacts. Then (25) defines a linear operator or matrix we denote as $\underline{\underline{\mathbf{G}}}$, transforming the coordinates of $\mathbf{U}$ into those of $\mathcal{U}$:

$$\mathcal{U} = \underline{\underline{\mathbf{G}}} \cdot \mathbf{U}. \tag{26}$$

$\underline{\underline{\mathbf{G}}}$ is the *rigidity matrix*, with N_f columns and DN_c lines, attached to the structure and geometry of the contact network. Note that the elements of $\underline{\underline{\mathbf{G}}}$ contain normal unit vectors and semi-branch vectors, and pertain therefore to one specific set of grain positions and orientations. The *kernel* of the rigidity matrix, $\ker \underline{\underline{\mathbf{G}}}$, is the subspace of $\mathbb{R}^{N_f}$ containing the coordinates of *mechanism motions*, i.e., those displacements and rotations causing no relative displacement at contacts. It may include some (a small number in usual applications) trivial such motions, in which the whole grain assembly moves as one rigid body. Its dimension, which we denote as κ, is the degree of displacement (or velocity) indeterminacy, or degree of hypostaticity. The *range* of $\underline{\underline{\mathbf{G}}}$, $\mathcal{R}\left(\underline{\underline{\mathbf{G}}}\right)$, is the subset of $\mathbb{R}^{N_c}$ containing the normal and tangential components of *compatible* relative displacements, i.e. those values which are actually achieved for some displacements and rotations of the grains. By the rank theorem, the dimension of $\mathcal{R}\left(\underline{\underline{\mathbf{G}}}\right)$ – the rank of matrix $\underline{\underline{\mathbf{G}}}$ – is $N_f - \kappa$.

Contact forces, defined in each contact as the forces exerted by the first grain onto the second one, may also be gathered in a DN_c-dimensional vector $\mathcal{F}$, with normal and tangential components in the same order as in vector $\mathcal{U}$. Forces and torques may be externally applied onto the grains, and their coordinates may be suitably gathered into an N_f-dimensional *load vector* $\mathbf{F}^{\text{ext}}$ – such that its work in small displacement $\mathbf{U}$ is simply the scalar product $\mathbf{F}^{\text{ext}} \cdot \mathbf{U}$. The equilibrium condition, for forces and torques, requests that $\mathbf{F}^{\text{ext}}$ is balanced by the net internal forces and torques on each grain, the coordinates of which form vector $\mathbf{F}^{\text{int}}$. It is easy to check that this condition simply writes

$$\mathbf{F}^{\text{ext}} = -\mathbf{F}^{\text{int}} = {}^{\mathbf{T}}\underline{\underline{\mathbf{G}}} \cdot \mathcal{F} \tag{27}$$

involving the transposed rigidity matrix. The kernel of ${}^{\mathbf{T}}\underline{\underline{\mathbf{G}}}$ contains all those sets of contact forces in equilibrium without any applied load – self-balanced contact forces. Its dimension H is the degree of force indeterminacy or degree of hyperstaticity of the contact structure. The range of ${}^{\mathbf{T}}\underline{\underline{\mathbf{G}}}$ contains all load vectors which may be balanced by some set of contact forces: it is the set of supportable loads (defined here without any sign or inequality condition on forces). The statement that the matrices appearing in (26) and (27) are transposed to each other is some kind of generalized theorem of virtual work: work may be evaluated as $\mathbf{F}^{\text{ext}} \cdot \mathbf{U} = \mathcal{F} \cdot \mathcal{U}$ whatever the choice of those vectors provided $\mathcal{U} = \underline{\underline{\mathbf{G}}} \cdot \mathbf{U}$ and $\mathbf{F}^{\text{ext}} = {}^{\mathbf{T}}\underline{\underline{\mathbf{G}}} \cdot \mathcal{F}$. Since the range of a matrix is the orthogonal complementary subspace to the kernel of its transpose, this provides a condition for compatibity of $\mathcal{U}$ (orthogonality to all sets of self-balanced contact forces) and a condition for supportability of $\mathbf{F}^{\text{ext}}$ (orthogonality to all mechanism motions). Finally, combining the relations on subspace dimensions stemming from the rank theorem and from $\mathcal{R}\left(\underline{\underline{\mathbf{G}}}\right) = \left[\ker {}^{\mathbf{T}}\underline{\underline{\mathbf{G}}}\right]^{\perp}$, one finds the following relation between H, the degree of hyperstaticity (force indeterminacy) and K, the degree of hypostaticity (velocity indeterminacy):

$$N_f + \text{H} = DN_c + \text{K}. \tag{28}$$

Variants of relation 28 apply to frictionless grains, for which only normal relative displacements and contact forces are relevant. Restricting accordingly the definition of the rigidity matrix and the appropriate spatial dimensions, one finds

$$N_f + \text{H} = N_c + \text{K}. \tag{29}$$

In the presence of rolling and pivoting resistance in the contacts, relative displacements are to be supplemented with relative rotations, and contact

forces are to be supplemented with contact torques, thereby increasing the number of lines of matrix $\underline{\underline{\mathbf{G}}}$ to $D(D+1)N_c/2$ (i.e. $3N_c$ in 2D and $6N_c$ in 3D). And (28) becomes

$$N_f + \mathrm{H} = \frac{D(D+1)}{2} N_c + \mathrm{K}. \tag{30}$$

Contact structures devoid both of hyperstaticity ($\mathrm{H} = 0$) and of hypostaticity ($\mathrm{K} = 0$) are *isostatic*. Equivalently, matrix $\underline{\underline{\mathbf{G}}}$ is square and invertible. It is also customary to regard as isostatic networks those that only possess trivial mechanism motions (global rigid body motions, or rotations for frictionless spheres) which are easily eliminated from the list of degrees of freedom. Note that isostatic systems have specific value of the coordination number, obtained on writing $N_c = zN/2$ and $N_f = D(D+1)N/2$, for N grains, in (28).

Properties. One fundamental characteristic feature of granular materials is the scarcity of contacts, which in some particular cases reaches the limit that the contact network becomes devoid of hyperstaticity ($\mathrm{H} = 0$). This is in particular, the generic case with frictionless grains in the rigid limit, i.e., when the confining stress is small enough and/or the stiffness of contacts large enough for the elastic deflections to be negligible – a condition that will be specified in more quantitative terms in the following. The absence of force indeterminacy for rigid frictionless objects, as discussed, e.g., by Roux (2000), is well established in generically disordered systems (Silbert et al., 2002; O'Hern et al., 2003; Agnolin and Roux, 2007a; Donev et al., 2007) and stems from the impossibility (in the statistical sense of events of vanishing probability) of satisfying specific relations involving grain positions and sizes. A familiar example is that of a four-legged table, which is generically wobbly on a hard floor – thereby suppressing force indeterminacy. As a property originating in geometric genericity, it applies to the contact network of hard grains, with or without friction: generically, self-balanced sets of normal contact forces cannot be supported. This entails an upper bound to the number of contacts in assemblies of rigid grains. Applying relation (29) to large contact networks, and eliminating rattlers (which would contribute $6x_0N$ to both N_f and K), one has $N_f = 6N$ (or $N_f = 3N$ in 2D), while N_c is equal to $z^*N/2$. Upper bounds on z^* follow: $z^* \leq 12$ ($z^* \leq 6$ in 2D) in general. If a lower bound is known to K, then the upper bound on z^* will be more stringent. With frictionless spheres (or disks) all rotations are mechanism motions, whence $\mathrm{K} \geq 3N$ and $z^* \leq 6$ (or $\mathrm{K} \geq N$ and $z^* \leq 4$ in 2D). With objects of revolution, $\mathrm{K} \geq N$ and $z^* \leq 10$. These bounds on (rattler-corrected) coordination number z^* ap-

ply, as already mentioned, to frictional objects in general. The isostatic value of z^* for frictionless objects coincides with this upper bound. Considering truly frictionless rigid objects, it is established (Roux, 2000) that the force-carrying structure in sphere assemblies under a certain load is isostatic ($\mathrm{K} = \mathrm{H} = 0$), while a non-vanishing degree of hypostaticity ($\mathrm{K} > 0$) may be retained in stable packs of frictionless grains of other shapes (which still satisfy $\mathrm{H} = 0$), as, e.g., ellipsoids (Donev et al., 2007). In the presence of friction, values well below the upper bound might be obtained. From (28), the isostatic value is $z^* = 4$ ($z^* = 3$ in 2D), whatever the grain shape. In general, contact structures of frictional objects are observed to possess little or no hypostaticity [the small proportion of spheres maintained between 2 contacts (Roux, 2000) is an exception], whence a lower bound: $z^* \geq 4$. The isostatic value is not very closely approached (one typically obtains $z^* = 4.5$ in poorly coordinated sphere assemblies), except on choosing unphysically large friction coefficients ($\mu \to \infty$) (Agnolin and Roux, 2007a). However, with ratio H/N_f of order 15%, it may be concluded that the paucity of contacts remains an important characteristic of granular materials. It explains the wide distribution of force values. While elasticity, which rules the distribution of forces in well connected networks, tends to share them evenly, geometrically determined force values, as modeled in some statistical approaches (Radjaï, 2015) tend to spread force values over wider intervals. With contacts capable of resistance to rolling and pivoting, it is easy to

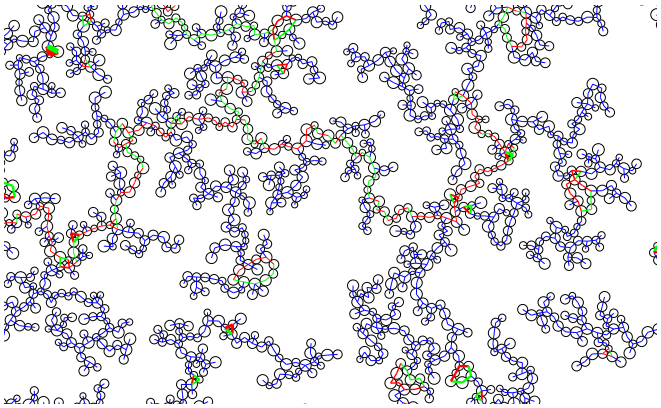

Figure 23. Detail of nearly loopless structure formed on slowly assembling cohesive grains with rolling resistance in the contacts (Gilabert et al., 2007).

show that any continuous contact network is devoid of non-trivial mechanism motion, any chain of contacting grains forms a solid structure (see

Fig. 10). In agreement with (30), the isostatic coordination number is equal to 2, the value characterizing a tree or loopless structure. Any cycle in the contact network creates hyperstaticity. Upon assembling, with adhesive grains, equilibrium contact networks by some dynamical process, loops will spontaneously appear as preassembled structures break and come into contact with one another. But if the assembling process is gentle enough, adhesive contacts will not break, and, as cycles only form in the unlikely event of two rigid structures coming in contact simultaneously by two different points, loopless, isostatic structures will tend to form, as shown in Fig. 23.

Rigidity matrix and stiffness matrix. The *rigidity matrix* and its transpose are objects of constant use in numerical computations of granular micromechanics: while equations of motion are written for the coordinates of $\mathbf{U}$, involving those of $\mathbf{F}^{\text{ext}}$ and $\mathbf{F}^{\text{int}}$, the contact behavior relates $\mathcal{F}$ to $\mathcal{U}$; matrix $\underline{\underline{\mathbf{G}}}$ and its transpose relate $\mathcal{U}$ to $\mathbf{U}$ and $\mathbf{F}^{\text{int}}$ to $\mathcal{F}$. *Stiffness matrices* express the response of the whole grain collection to small displacements. They are mostly used in quasistatic conditions (although they might also contain some viscous terms associated with wave damping). Their relation to rigidity matrices is explicitly shown here, for elastic contact behavior: small changes in relative displacements $\Delta\mathcal{U}$ are assumed to correspond to small contact force increments $\Delta\mathcal{F}$ as

$$\Delta\mathcal{F} = \underline{\underline{K}} \cdot \Delta\mathcal{U}, \tag{31}$$

where the *local stiffness matrix* $\underline{\underline{K}}$, a square matrix of order DN_c, expressing contact elasticity, contains zeros except on its principal diagonal, the elements of which are the normal and tangential stiffnesses K_N and K_T for all the contacts (values of K_N and K_T depend on the contact geometry and its deflection). Using the rigidity matrix, $\Delta\mathcal{U}$ results from small displacements and rotations, coordinates of $\Delta\mathbf{U}$; and the increment in the net forces and torques on the grains, $\Delta\mathbf{F}^{\text{int}}$, results from $\Delta\mathcal{F}$:

$$\Delta\mathbf{F}^{\text{int}} = -\,{}^{\mathbf{T}}\underline{\underline{\mathbf{G}}} \cdot \Delta\mathcal{F} = -\,{}^{\mathbf{T}}\underline{\underline{\mathbf{G}}} \cdot \underline{\underline{K}} \cdot \Delta\mathcal{U} = -\,{}^{\mathbf{T}}\underline{\underline{\mathbf{G}}} \cdot \underline{\underline{K}} \cdot \underline{\underline{\mathbf{G}}} \cdot \Delta\mathbf{U} = -\underline{\underline{\mathbf{K}}} \cdot \Delta\mathbf{U}$$

This defines the *stiffness matrix* of the granular sample, a square matrix or order N_f, $\underline{\underline{\mathbf{K}}}$, as

$$\underline{\underline{\mathbf{K}}} = {}^{\mathbf{T}}\underline{\underline{\mathbf{G}}} \cdot \underline{\underline{K}} \cdot \underline{\underline{\mathbf{G}}}. \tag{32}$$

$\underline{\underline{\mathbf{K}}}$ is symmetric if $\underline{\underline{K}}$ is symmetric (which is insured by its diagonal form in the elastic case), and positive if $\underline{\underline{K}}$ is positive (as for elastic contacts with $K_N > 0$ and $K_T > 0$). If $\underline{\underline{K}}$ is diagonal with non-vanishing elements, the

Table 1. Influence of initial state and dimensionless control parameters on mechanical behavior (Y=Yes, N=No)

	initial state	I	κ ($> 10^3$)	e or ζ	μ, $\mu_{R,P}/a$	P^*
Assembling	Y	Y	N	Y	Y	Y
Quasistatic (I)	Y	N	Y	N	Y	Y
Quasistatic (II)	Y	N	N	N	Y	Y
Critical state	N	N	N	N	Y	Y
Dense flow	N	Y	N	N	Y	Y
Collisional	N	Y	N	Y	Y	Y

kernel of $\underline{\underline{\mathbf{K}}}$ coincides with the kernel of $\underline{\underline{\mathbf{G}}}$, i.e., contains the mechanism motions. Stiffness matrices are used to numerically measure elastic moduli and discuss theoretically their values and relations to microstructure (Agnolin and Roux, 2007c; La Ragione and Jenkins, 2007). In case the force in some of the contacts reaches the Coulomb threshold, causing potential sliding, one may still express the elastoplastic response through a local stiffness matrix coupling. $\underline{\underline{K}}$ remains block-diagonal, with 3×3 ($D \times D$) blocks corresponding to each contact, possibly coupling tangential forces to normal displacements for contacts with full friction mobilization – this matrix now depends on the direction of incremental displacements (McNamara and Herrmann, 2006; Roux and Combe, 2011). Such elastoplastic stiffness matrices are useful in the study of quasistatic contact network response and stability (Roux and Combe, 2002; Welker and McNamara, 2009; Roux and Combe, 2011).

3.4 Dimensionless control parameters

In view of the potential complexity of contact behavior, it has proved useful to extract the essential parameters governing material behavior in dimensionless form (Roux and Chevoir, 2011). Such dimensionless groups combine parameters appearing in contact laws (such as material elastic properties) and those defining the mechanical test one wishes to model. Measurements of granular rheology typically involve some stress control, say some pressure level P, and some strain rate $\dot{\varepsilon}$ – with plastic-like response for small enough rates, and different states away from mechanical equilibrium in flow.

Table 1 summarizes the dependence of material behavior in different regimes on control parameters. One relevant classification of the different regimes of mechanical behavior of granular materials is in terms of solid-like (statically resisting shear stress) or liquidlike (flowing) rheology, supplemented, by analogy with collections of molecules, with the case of "granular

gases", in which the grains are strongly agitated and interact with one another in sequences of collisions. These categories correspond, in part, to the lines of Table 1. The columns are labelled according to the different relevant dimensionless parameters, and the intersection of, *e.g.*, column μ (together with rolling or pivoting friction coefficients in dimensionless form), contains "Y" on all lines for which μ (μ_R and μ_P as well) have some influence on the material behavior in the situation considered. Friction coefficients turn out to affect all rheological regimes.

The inertial number, I, quantifies the distance to equilibrium by multiplying $\dot{\varepsilon}$ by a characteristic time. Let us consider one grain, of diameter a and mass m, in interaction with its neighbours by contact forces that may vary as the material deform and the contact network rearranges. The net force, accelerating it, is of order Pa^2. New contacts will form within some inertial time τ_i, of the order of the time within which the grain, accelerated from rest, moves some distance proportional to a, i.e. $\tau_i = \sqrt{m/aP}$. One may thus define a dimensionless strain rate or *inertial number* as

$$I = \dot{\varepsilon}\sqrt{\frac{m}{aP}}. \tag{33}$$

(Some use variant $I = a\dot{\varepsilon}\sqrt{\rho/P}$, ρ being the mass density within the grain).

The quasistatic limit, in which the material behaves like a solid, is the limit of $I \to 0$. A definition might depend on the accuracy with which inertial effects and kinetic energy may be neglected. In practice, for simple systems (e.g., frictional spherical beads with narrow diameter distribution), a solid regime is achieved below $I = 10^{-3}$ or 10^{-2}. Frictionless grains require smaller values for the quasistatic behavior to be approached (Peyneau and Roux, 2008a). This defines the "quasistatic" lines of the table. In such regimes, I, by definition, becomes irrelevant, and so are the viscous forces – whence the "N" in the column corresponding to viscous damping (ζ) or restitution coefficients (e). Such ingredients of the contact model turn out to have little influence in dense granular flows too, i.e., in the regime of I values up to order 0.1 (da Cruz et al., 2005). But more strongly agitated systems are sensitive to the level of dissipation in collisions (e or ζ).

Contact forces, under pressure P, or of order Pa^2 (with some effect of density and coordination, see relation 20). With Hertzian contacts, this entails some deflection h of order $[Pa^2/(a^{1/2}\tilde{E})]^{2/3}$, from (3). Comparing h to diameter a defines a stiffness number:

$$\kappa = \left(\frac{\tilde{E}}{P}\right)^{2/3}, \tag{34}$$

such that $(h/a) \propto \kappa^{-1}$, quantifying the geometric effect of contact deflection. The limit of rigid grains is defined as that of $\kappa \to \infty$. With usual materials (say, for sands or glass beads), κ usually remains above 10^3, unless grains are subjected to such high pressures that the stress concentration in contact regions should cause breakage (Agnolin and Roux, 2007b). h/a may be regarded as an order of magnitude for macroscopic strains, if their microscopic origin is the material strain in the contact regions. Anticipating on Sec. 5.1, such a strain regime is referred to as "type I" in Tab. 1, while strains associated to contact network rearrangements – as in the simple example of Fig. 17 – are termed "type II strains". Type I strains are naturally of order κ^{-1}, while larger strain scales, within a solidlike quasistatic regime, are insensitive to κ if $\kappa > 1000$. With linear contact elasticity, involving a constant stiffness parameter K_N, κ is appropriately defined as $K_N/(aP)$.

Column P^*, in Table 1, concerns cohesive materials, for which force scale F_0 (the tensile strength, introduced in connection with Eq. 6 and Fig. 9) should be compared to confining forces of order Pa^2. This defines a reduced pressure, P^* (last column in the table), as

$$P^* = \frac{a^2 P}{F_0}. \tag{35}$$

Cohesive effects dominate for $P^* \ll 1$ and become negligible for $P^* \gg 1$. Intergranular adhesion stabilizes open structures as shown in Figs. 10 and 23. For growing P^* such structures collapse, and as F_0 becomes negligible, the dense force networks of Fig. 15 are retrieved.

The assembling process by which granular samples are prepared, before rheological tests are carried out, is both important and little known, because models of granular materials have been focussing on solid deformation or steady flow, whereas assembling processes are inherently hybrid situations, in which agitated or flowing materials come to rest in a short time. It tends to depend on all factors and parameters mentioned in the table, and is briefly discussed in the next section.

4 Assembling process and compression.

The assembling processes condition the initial states of granular materials prior to mechanical testing. Most frequently such processes should include a compression stage, which brings the material to a certain controlled prestressed state. Unlike ordinary solids such as metals, granular materials have no natural state independently of the confining stress. The classical approaches to the mechanics of solidlike granular materials describe their response to *changes* or *increments* of external stress. Assembling methods

escape such models as elastoplasticity applied to soil mechanics, and the knowledge of these processes is still largely empirical. For cohesionless materials, the method of *controlled pluviation* offers the advantage to produce homogeneous samples of varying densities. It consists in raining grains onto the free surface of a growing sample (Rad and Tumay, 1987; Benahmed et al., 2004), with constant flow rate per surface area and constant vertical velocity of the falling grains. Simulations (Emam et al., 2005) enable homogeneity checks. Fig. 24 shows the lack of homogeneity due to a varying height of free fall during the sample fabrication.

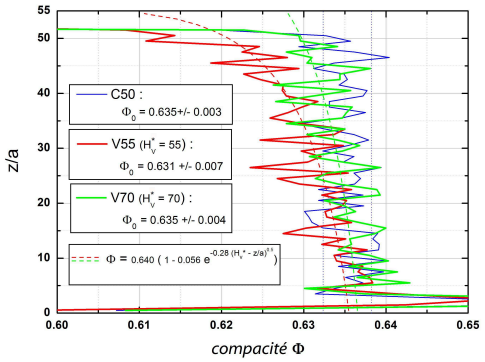

Figure 24. Vertical solid fraction profile $\Phi(z)$ in DEM-simulated samples assembled by pluviation. Blue line (C50): homogeneous system assembled with constant height of free fall H. Red (V55) and green (V70) lines: varying Φ obtained on dropping grains from constant elevation. Dotted lines: model of such variations from H-dependent controlled pluviation results.

Many assembling processes have been tested by DEM (Combe and Roux, 2011). They are often simply characterized by the values of the final state variables, rather than striving to mimic laboratory methods. The slow compression of loose configurations with initially non-contacting grains, until a contact network resists further compression, is a convenient method if carried out homogeneously within a periodic box of decreasing size. This results in a variety of microstructures, hopefully representative of the possible material states under low stresses. In the following, results will be reported on such ideal structures, initially isotropic. Specifically, we briefly report on the salient results obtained by Agnolin and Roux (2007a,b,c) on various isotropic states: very dense, highly coordinated states (denoted as A), with $\Phi_A \simeq 0.64$ and $z_A^* = 6$ under low pressure (RCP state); very dense, poorly coordinated ones (denoted as C) with $\Phi_C \simeq \Phi_A$, but $z_C^* \simeq 4.6$; intermediate

ones (B) such that $\Phi_B \simeq 0.628$ and $z_B \simeq 5.8$; and looser ones (D), with $\Phi_D \simeq 0.593$ and $z^*_D \simeq 4.55$. (These values are obtained under low pressure, corresponding to $\kappa \simeq 39000$, or glass beads under 10 kPa). Among these systems those with low coordination initially have a proportion x_0 of rattlers above 10%. A result of DEM studies (unknown in the previous literature on dense bead packs) is thus the existence of very dense states with low coordination numbers, as z^*_C is not larger than z^*_D, while Φ_C is very close to the maximum value of RCP. As to state B, it is looser than C, but better coordinated. Although the process leading to states A and B could be argued to be similar to lubricating the grains (ideally for A, assembled with $\mu = 0$, imperfectly for B) and the preparation of C bears some analogy to vibrating grains in a dense configuration, for lack of accurate measurements of coordination numbers in large grain assemblies it is not known in general which value of z^* corresponds to experimental dense bead packs.

Fig. 25 shows the evolution of density and coordination in such systems under an isotropic compression cycle, along with the shape of the force dis-

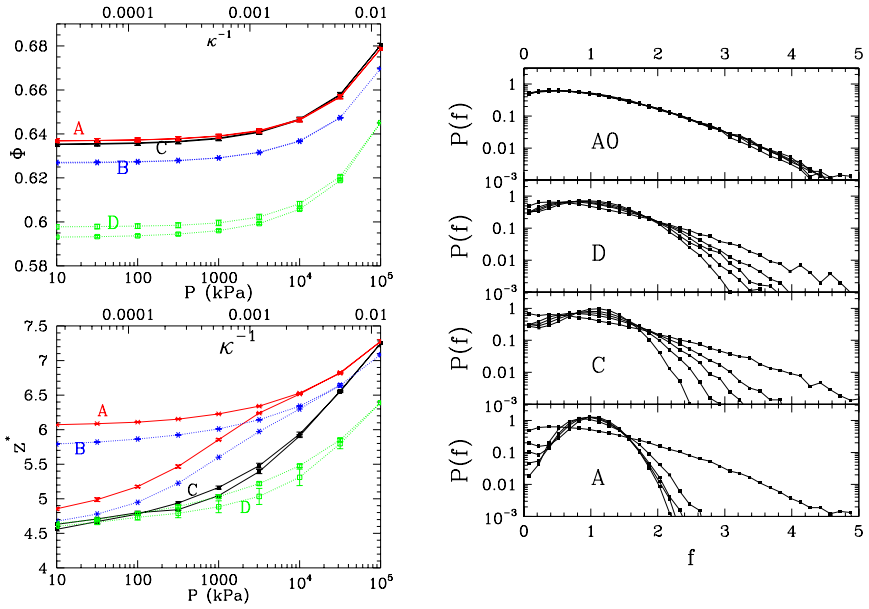

Figure 25. Left: variations of Φ and z^*. Right: distribution of normal forces, normalized by their averages (Agnolin and Roux, 2007b), for 5 values of P, κ decreasing from 39000 to 84 by factors of $10^{2/3}$. A0-labelled results correspond to A systems kept frictionless during the compression.

tribution, normalized by average $\langle F_N \rangle$ (or distribution of $f = F_N/\langle F_N \rangle$). The friction coefficient is equal to 0.3 in all cases. Changes in Φ and z^* are moderate as long as $\kappa > 10^3$ (although more notable for z^* when initially low). The growing force indeterminacy as z^* increases well above the minimum value 4 leads to gradual narrowing of distribution $P(f)$ – quite fast in system A, for which friction is "plugged in" at the lowest pressure, and slowly in frictionless case A0, which remains close to isostatic over a large pressure range. Remarkably, the evolution of Φ in the pressure cycle is almost reversible (with the small difference between A and C retrieved upon decompressing). Sands are supposed to behave plastically, with a significant density increase under isotropic compression. The different DEM observations are very likely due to the absence of damage in the contact regions in the numerical model. On the other hand, it is quite remarkable that the coordination number, if initially high, decreases by a large amount in the compression cycle (Fig. 25) – a phenomenon that occurs even for smaller pressure cycles. The reversibility is only apparent, and complex contact network evolutions take place. *Oedometric* compression (Khalili et al., 2017), in which σ_1 is increased with no lateral strain ($\varepsilon_2 = \varepsilon_3 = 0$) reveals a similar behavior to isotropic compression.

Cohesive systems, as announced in Sec. 3.4, if initially stabilized in very loose structures (Gilabert et al., 2007; Than et al., 2017), as apparent in Figs. 10 and 23, will irreversibly collapse to denser states under growing stress intensity. Their plasticity in isotropic (or oedometric) compression,

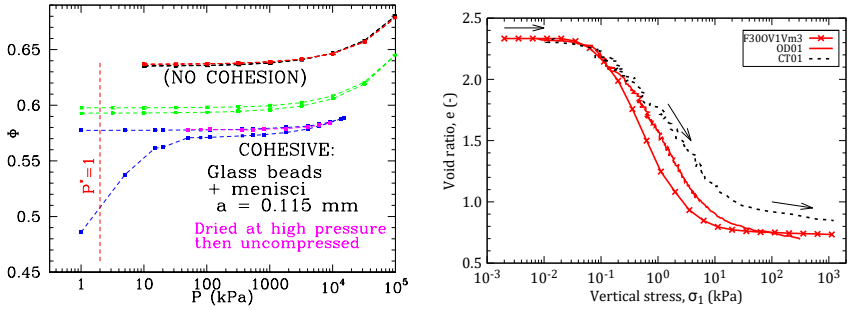

Figure 26. Left: Φ versus P in model wet bead assemblies, comparing systems with and without capillary cohesion. Right: Void index $e = -1 + 1/\Phi$ versus pressure in experiments (red solid line and black dashed one for a different test) and simulations (red connected points) with wet beads (Than, 2017) of diameter 0.1 mm.

unlike the subtle and hidden irreversible evolution of the model cohesionless systems of Fig. 25, is very conspicuous. Fig. 26 shows the simulated behavior of wet glass beads, attracting one another at contacts through small liquid bridges as in Fig. 8. Most of the irreversible density increase occurs in P^* range between 0.1 and a few units. Note that the numerical observations (right graph) are similar to experimental ones (Than, 2017), despite a certain lack of reproducibility of the latter.

Loose cohesionless systems might be obtained on suppressing capillary cohesion (as if drying, or, equivalently for the solid, quasistatic behavior, saturating the system) under large P^*, and then decompressing to a low pressure (see first graph of Fig. 26). Still using $\mu = 0.3$, one thus gets samples denoted as L, with $\Phi = 0.571 \pm 0.005$ and $z^* \simeq 4.7$.

5 Quasistatic behavior

We now turn to the response of solidlike granular systems in classical mechanical tests. Illustrations mainly focus on triaxial compressions of the cohesionless model material (assemblies of spherical beads, $\mu = 0.3$) the preparation of which in different states is presented in Sec. 4. What do we learn from the study of such materials in triaxial compression, with the full microscopic information accessible in numerical, grain-level modeling via DEM? The results reported here aim at clarifying (Sec. 5.1) the role of elasticity and the deformation mechanisms of granular materials, depending on their initial state, which should not only be classified according to its density. We also relate the approach of the critical state at large strain with internal material state evolutions (Sec. 5.2).

5.1 Initial state, small strains, "prepeak" behavior

Initial elastic behavior. Pressure dependent elastic moduli, in isotropic compression, might be obtained using the elastic stiffness matrix of Sec. 3.3. Fig. 27 shows the values of the bulk (B) and shear (G) moduli of the isotropic systems of Fig. 25, versus pressure. It should be remarked that the values of moduli are more sensitive to coordination number z than to density: well-coordinated systems A and B are separated from poorly coordinated ones C and D (even though C is denser than B). Elastic moduli, which may be measured in the laboratory, may thus be regarded as indirect measurements of coordination number. It is expected from relations 4 and 20 that moduli grow as $P^{1/3}$. Best linear fits on the logarithmic graphs of Fig. 27 give however somewhat larger exponents. To some extent, this is due to the increase of the contact density in compression (variation of z,

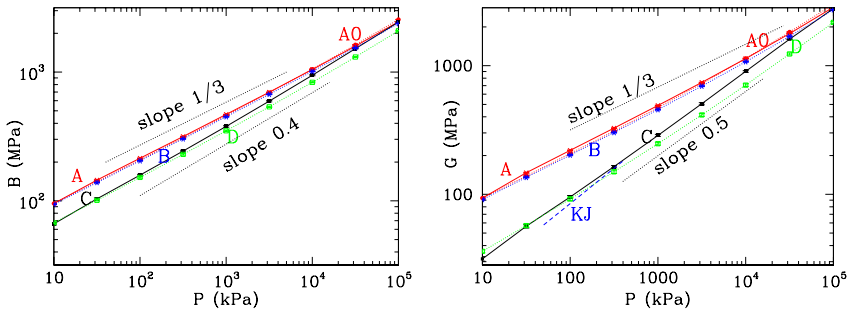

Figure 27. Elastic moduli in the different systems of Fig. 25 in isotropic compression [from Agnolin and Roux (2007c)]. Data set marked "KJ" correspond to experimental results on loose pack of glass beads (Kuwano and Jardine, 2002). Left: B versus P. Right: G versus P.

see Fig. 25). However, this does not explain the different behavior of shear moduli, which are anomalously small in poorly coordinated systems. This peculiar behavior is reflected by the performance of the Voigt approximation for the moduli, based as usual on the assumption that displacements associated to macroscopic strain $\underline{\underline{\varepsilon}}$ coincide with the values of the corresponding affine field at grain centres. This approximation predicts values B^{V}, G^{V}, in-

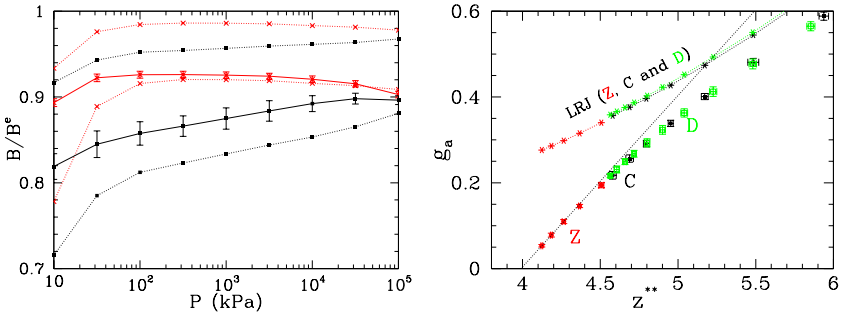

Figure 28. [From Agnolin and Roux (2007c)] Left: ratio B/B^e (data points with error bars, joined by solid line), with B^e defined in (36), bracketed by Voigt (crosses) and Reuss (square dots) estimates, in A (red) and C (black) states versus P. Right: G, normalized by average contact stiffness and density, versus corrected z^* value. "Z" data points: samples with $\mu = \infty$. "LRJ" points: prediction of model by La Ragione and Jenkins (2007) .

volving the constant stiffness ratio α_T defined in (5) and $Z(1/3) = \frac{\langle F_N^{1/3} \rangle}{\langle F_N \rangle^{1/3}}$, characteristic of the force distribution:

$$B^{\mathrm{V}} = Z(1/3)B^e = \frac{1}{2} Z(1/3) P^{1/3} \left(\frac{z\Phi\tilde{E}}{3\pi} \right)^{2/3} ; G^{\mathrm{V}} = \frac{6 + 9\alpha_T}{10} B^{\mathrm{V}}. \quad (36)$$

The Voigt approximation grossly overestimates G especially for small z. The explanation was first contributed by Wyart (2006), who argued that G should be proportional to the degree of hyperstaticity. On the other hand, B, because it expresses the response to a stress increment proportional to the preexisting stress, possesses a Reuss-like lower bound (Agnolin and Roux, 2007c), obtained from trial force increments proportional to the preexisting forces. This Reuss estimate is also proportional to B^e defined in (36). Thus the bulk modulus is bracketed in some satisfactory estimation interval (Fig. 28). The second graph of Fig. 28, in which shear moduli, divided by obvious factors of average stiffness and density, are plotted versus z^{**} (a slightly corrected value of z^* such that the degree of hyperstaticity H is proportional to $z^{**} - 4$) shows that the shear modulus indeed tends to vanish proportionally to degree of hyperstaticity H (Somfai et al., 2007; Agnolin and Roux, 2007c). To explore this tendency, additional samples with infinite friction coefficients were assembled by Agnolin and Roux (2007c), in which $z^{**} = 4$ is approached at low pressure. The model by La Ragione and Jenkins (2007), a sophisticated self-consistent approximation scheme, provides improved estimates of G but fails to capture its tendency to vanish proportionally to H.

Prepeak behavior and initial coordination number. With initial isotropic state C, compressed to different pressures, the prepeak behavior, expressed with stress ratios and strains, as shown in Fig. 29, shows little dependence on initial pressure P. The peak deviator is reached for $\varepsilon_a \sim 3.10^{-2}$. But, of course, on much smaller scale, one should first observe, close to the initial state, the quasielastic regime. The corresponding strain interval, shown in the insets of the graphs of Fig. 29, is of order 10^{-6} to 10^{-4}, as in experiments on sands. The moduli, as deduced from the stiffness matrix approach, based on the assumption of a stable contact network in which all contacts behave elastically, describe the initial slope of stress-strain curves. This quasi-elastic regime is observed (Agnolin and Roux, 2007c) to grow approximately as $P^{2/3}$, which, assuming moduli proportional to $P^{1/3}$, would correspond to constant relative stress increments $\delta\sigma/\sigma$.

Interestingly, elastic moduli may also be measured for different states along the curves of Fig. 29. The stress deviator increase along the curve

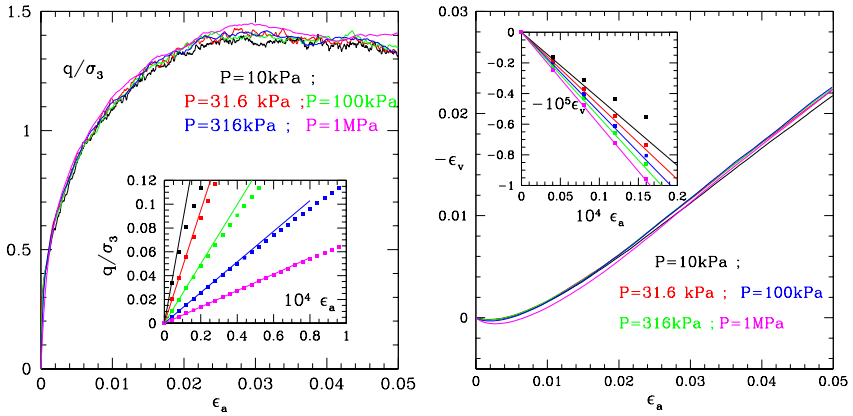

Figure 29. Deviator stress normalized by constant lateral stress q/P, in prepeak regime (left), and volumetric strain (right) versus axial strain, in dense initial states with small coordination number (C), for different values of P, and elastic properties of glass beads. Insets: initial quasielastic regime (note blown-up strain scale), straight line slope given by Young modulus (left) or $-(1-2\nu)$ (right).

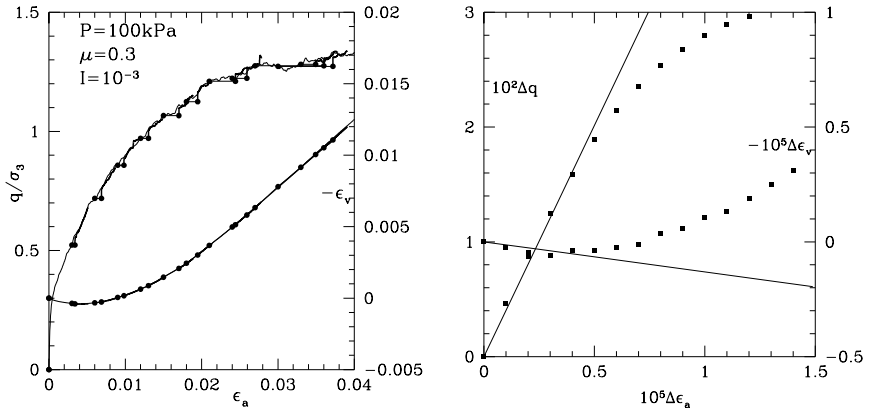

Figure 30. Left: creep to equilibrium (between dots) and resumed compression test along triaxial loading path. Right: resumed, strain rate controlled, triaxial compression (dots). Straight line slopes given by elastic moduli.

reflects a non-elastic behavior, because of friction mobilization and network restructuring. On maintaining constant stresses, rather than imposing the axial strain rate, small creep strain intervals are observed, leading to well-equilibrated states. Those states, in which contact networks are stabilized with force values without full friction mobilization, first respond elastically upon resuming the imposed strain rate test. Such elastic properties reflect

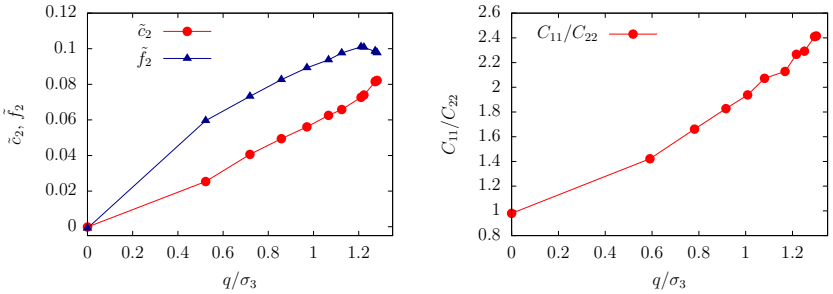

Figure 31. Growing anisotropy in triaxial test for dense (C-type) initial state: $\tilde{c}_2 = 4b_2/15$ and $\tilde{f}_2 = 4b_2^N/15$ (left); C_{11}/C_{22} (right) versus q/σ_3.

the growing anisotropy of the systems in triaxial compression, as shown in Fig. 31. Thus the longitudinal moduli become larger in the axial direction (C_{11}), than in the transverse ones (C_{22}), because of the increasing fabric and force anisotropies. Contact normal directions are more numerous near the axial direction (with growing parameter b_2), and also tend to carry larger forces (b_2^N increases).

The dependence of the triaxial compression curve on the initial coordination number is visualized in Fig. 32, showing, on the same graph, the deviator and the volumetric strain curves obtained from initial states A and C, characterised by a very similar density (Φ near the maximum, RCP value) but different coordination numbers: z^* near 6 for A, about 4.6 for C (and $z \simeq 4$). While the height of the peak deviator stress, given the level of statistical uncertainty on measurements on finite samples (see right graph in Fig. 32), should be regarded as identical, the shape of the stress-strain curve is notably different, with a much steeper initial rise of deviator stress in the well coordinated system. Fig. 33, showing, analogously to Fig. 29, triaxial test results in A samples under varying initial pressure (and constant lateral stress) P, reveals a striking difference: strain amplitudes strongly vary with P for the part of the response corresponding to the steep increase of deviator stress. On rescaling strains, using the scale of elastic strains, proportional to $P^{2/3}$ (because moduli tend to grow like $P^{1/3}$), or like contact deflections

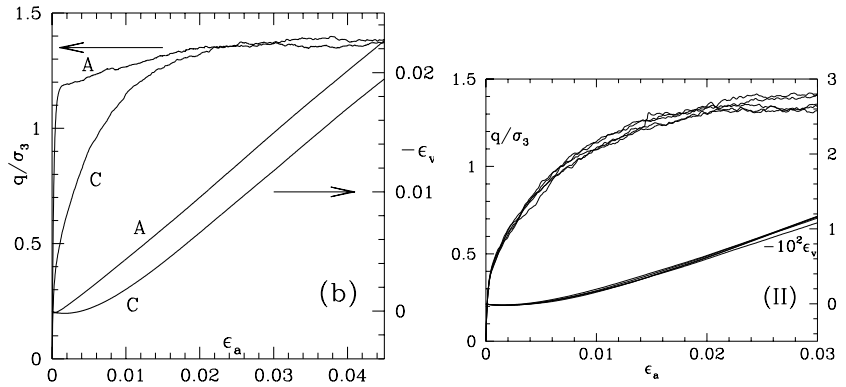

Figure 32. (Roux and Combe, 2010). Left: triaxial compression response for initial states A and C ($\kappa \simeq 8000$). Right: response of different C-type samples.

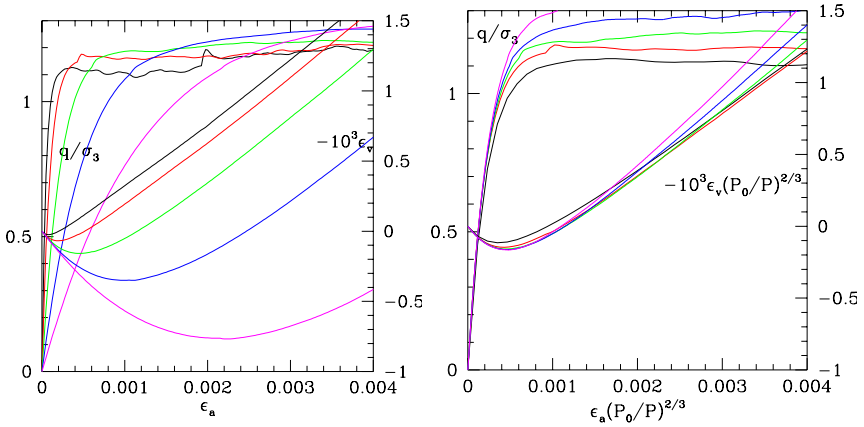

Figure 33. (Roux and Combe, 2010). Triaxial tests in dense systems A with initially large coordination number. Left graph: q/P and ϵ_v shown versus ε_a for different P. Right graph: same data, shown versus rescaled strain $\varepsilon_a(P_0/P)^{2/3}$.

$h/a \propto \kappa^{-1}$, thus using strain coordinates proportional to $\kappa\varepsilon$, then these different curves tend to superimpose in the initial range. This is characteristic of *type I strains*, which stem from strains in the contact regions: as long as q/P stays below 0.8 or 0.9, A-type systems deform because contact regions

deform. This contrasts with the type II strains exhibited by systems in initial state C, for which macroscopic strains are not sensitive to κ, as shown above with Fig. 29 and reported in Table 1. In a type I strain regime (Roux and Combe, 2002, 2010; Roux, 2015), the granular system actually behaves like a network of rheological elements as shown in Fig. 11. Although the strains are not elastic, due to intergranular friction (the plastic sliders in the network of rheological elements), elasticity (the springs) sets the strain scale. Within such type I regimes, the creation of new contacts plays a minor role: it is possible to observe the same behavior with simulations in which only the initial contact network is dealt with, as long as this network does not break. It is also possible to simulate this behavior with purely static methods, based on elastoplastic stiffness matrices (Welker and McNamara, 2009; Roux and Combe, 2011). Beyond regime I (say for $q/P > 1$ in systems A, and much sooner, for $q/P > 0.3$ in systems C) contact networks get repeatedly broken and repaired, in rearrangements involving instabilities at the microscopic scale. "Quasistatic" stress-strain curves are strictly continuous sets of equilibrium configurations in regime I. In regime II they have to be understood as discontinuous sets of equilibrium configurations involving jumps during which the system gets accelerated first, and then stabilizes with a new contact network. To obtain a macroscopic constitutive law from microscopic ingredients one should therefore follow different routes according to the type of strain. Regime II is more challenging, as the amplitude of strain does not originate in contact behavior, but in the complex geometry of rearranging grain packs.

Type I strains are observed for stable contact networks, and naturally extend to larger stress intervals for large coordination numbers (whence the behavior of A samples). They also occur over notable intervals on reversing the loading direction in tests such as the triaxial compression: load reversal, causing tangential forces to return inside the Coulomb cone, reduces the number of sliding contacts and may suppress the contact network instability due to friction mobilization. Systems with small hyperstaticity tend to possess less stable networks and typically exhibit type II response. In the extreme case of rigid, frictionless grains, forming contact networks with no force indeterminacy (isostatic for spheres or disks), it was explicitly shown (Combe and Roux, 2000) that the range of stability of equilibrium contact structures, in terms of stress interval, vanishes in the limit of large samples. Any stress increment, however small, causes a rearrangement and strains in the macroscopic limit. Frictionless grain assemblies (Peyneau and Roux, 2008a,b; Azéma et al., 2015), in which stress-strain curves are particularly elusive – non-existent, according to Combe and Roux (2000), if grains are perfectly rigid – exhibit finite macroscopic friction, but, at least for cir-

cular, spherical or polygonal shapes, are devoid of dilatancy, contradicting naive intuitions based on mechanisms like the one of Fig. 14. Instabilities, producing combined complex displacement fields as shown in Fig. 16, turn out to produce contraction as much as dilation (Combe and Roux, 2000; Azéma et al., 2015).

5.2 Larger strains and approach to critical state

Fig. 34 shows how initially isotropic states L, D and A, made of frictional beads ($\mu = 0.3$) assembled with solid fraction ranging from $\simeq 0.57$ (L) to 0.64 (A), approach the same critical state at large axial strain ε_a. As

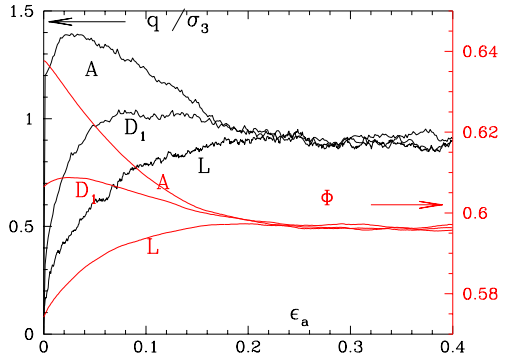

Figure 34. Deviator stress (left axis) and solid fraction (right axis) versus axial strain for dense (A), medium dense (D) and loose (L) initial state.

expected, all three initial states evolve towards the same plastic plateau value ($q_c/\sigma_3 \simeq 0.9$) for deviator stress and the same density (solid fraction $\Phi_c \simeq 0.595$) for axial strains above 0.3. With, initially, $\Phi_c < \Phi_D < \Phi_A$, systems A and D classify as dense: deviator stress, increasing with ε_a, goes to a maximum, the larger the denser the initial state, and then decreases to the critical plateau value q_c. Meanwhile, solid fraction Φ decreases (after some contractant initial phase for D) towards the critical value Φ_c. On the other hand, with $\Phi_L < \Phi_c$, initial state L classifies as loose: as axial strain ε_a grows, its solid fraction Φ, which decreases, and its deviator stress q, which increases, both vary monotonically and asymptotically approach their critical values, Φ_c and q_c, at large ε_a.

As apparent in Fig. 35, specific values for all internal state variables, which are common to different initial states, are approached for large strain

in monotonic triaxial compression – this confirms the existence of a well-defined critical *state*, with a specific *plastic flow structure*. The second graph

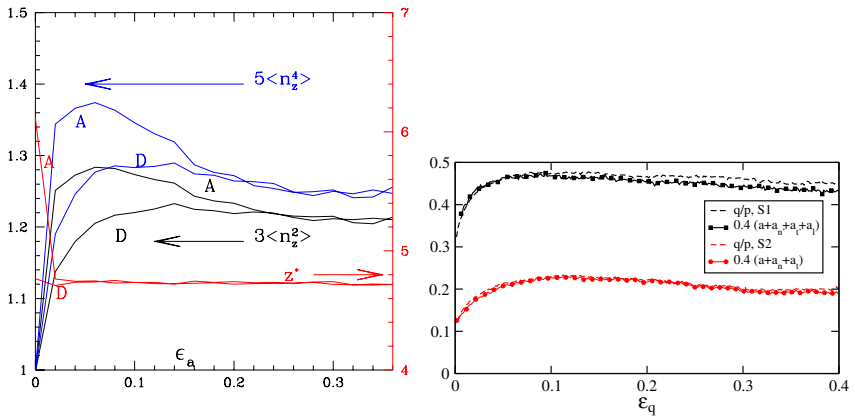

Figure 35. Left: Coordination number and fabric parameters versus axial in triaxial tests of Fig. 34 for initial states A and D. Right (Azéma et al., 2009): ratio $q/(3P+q)$ versus deviatoric strain $\varepsilon_q = \varepsilon_1 - \varepsilon_3$ (dashed lines) versus prediction of Eq. 24 (dots). Lower red curve: beads ($\mu = 0.5$); upper black curve: polyhedra ($\mu = 0.5$).

illustrates the success of approximation (24), relating stresses to leading fabric and force anisotropy parameters – suitably supplemented with adequate branch vector anisotropy parameter in the results on polyhedra given here, from Azéma et al. (2009).

The critical state thus acts as an *attractor* to which all initial states converge, after large enough monotonically growing strains. It has therefore to be included in constitutive modelling, as a central concept, and state parameters are often specified in terms of the distance to the critical state. Dilatancy, which vanishes in the critical state, may thus be related to some stress combinations (Wood, 1990). Plasticity models have been designed to account for specific fabric anisotropies, by which critical states are different, e.g., in simple shear or in triaxial compression (Manzani and Dafalias, 1997). The statement that the critical state, for a given loading direction, only depends on μ for cohesionless materials (and possibly on rolling and pivoting friction, if present) as made here in Table 1, is somewhat at odds with the tradition of soil mechanics, according to which the critical state volume fraction Φ_c (or the void ratio $e_c = -1 + 1/\Phi_c$) varies with pressure, on the so-called "critical state line". This classical behavior of sands is believed

however to be related to contact damage, which standard DEM approaches usually ignore– whence the essentially κ-independent behavior recorded in Fig. 29, as soon as ε_a exceeds the small range of regime I strains. The critical state internal friction coefficient increases with μ [from its initial value near 0.1 for $\mu = 0$, Peyneau and Roux (2008a)] but usually reaches a plateau for $\mu > 0.25$. As to Φ_c, the critical solid fraction, it coincides with the RCP value with frictionless spherical grains (which are devoid of dilatancy), and steadily decreases for growing μ (Lemaître et al., 2009). Due to its rheological importance (the material cannot be continuously sheared above Φ_c) and independence on preparation, the critical state has often been characterized in DEM, for varying grain shapes (Azéma et al., 2013), or size distributions (Voivret et al., 2009). Contact elasticity being irrelevant for large strains, such studies may be carried out using models of rigid grains, as implemented in the "Contact Dynamics" simulation method (Radjaï and Richefeu, 2009; Radjaï and Dubois, 2011).

6 Dense granular flow

Quasistatic critical states, in triaxial compression, or in simple shear, with controlled normal stress (as in Fig. 36), only depend on the friction coefficient. Steady dense flows, in which the material state departs notably from the quasistatic limit, may be regarded as generalizing critical states. Steady

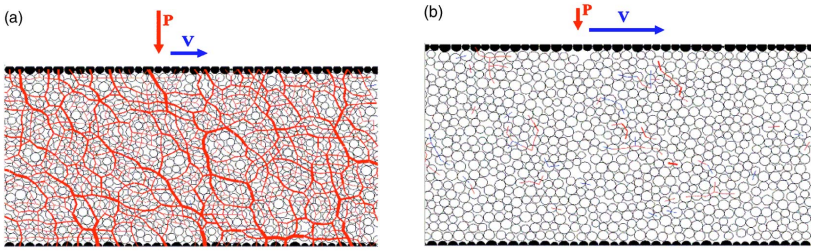

Figure 36. Sheared disk system, under controlled normal stress σ_{22} (denoted as P on the figure), with drawing of contact forces, with $I = 0.01$ (a) and $I = 0.2$ (b) (note volume change) (da Cruz et al., 2005).

uniform flows are most easily described in simple shear, with a velocity field in direction 1, constant gradient in direction 2, and controlled stress σ_{22}. Using shear rate $\dot{\gamma} = \frac{\partial v_1}{\partial x_2}$ to define the inertial number as in (33) (suppress diameter a in the denominator for an appropriate 2D definition), the state of the flowing material only depends on I, with the critical state in the

quasistatic limit of $I \to 0$. The change in the state of the flowing material

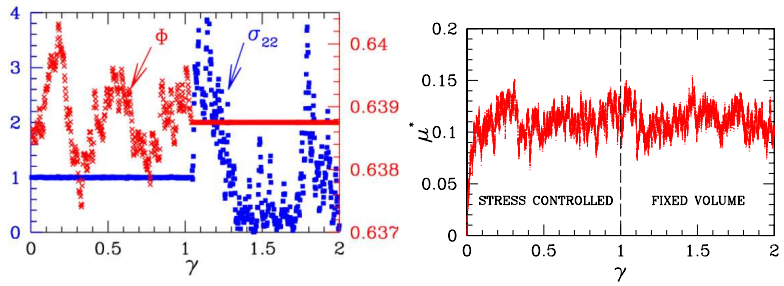

Figure 37. Left: normal stress σ_{22} (left axis) and Φ (right axis) in simulated shear flow of frictionless beads, versus shear strain γ. For $\gamma < 1$, $\sigma_{22} = 1$ is imposed, Φ fluctuates with average $\overline{\Phi} \simeq 0.6378$; for $\gamma > 1$, Φ is fixed at value $\overline{\Phi}$, σ_{22} fluctuates. Right: ratio $\mu^* = |\sigma_{12}|/\sigma_{22}$ versus γ.

with I is quite conspicuous in Fig. 36, as the "force chain" pattern of quasistatically deformed materials (similar to Fig 15, but with the characteristic anisotropy of shear flow) becomes much more tenuous for I in the 0.1 range, as the flowing systems dilates. The force network gradually evolves towards a set of binary interactions, isolated in space and time, in the collisional flow regime at larger I. Originated in soil mechanics, the idea to characterize flowing granular materials under controlled normal stress (da Cruz et al., 2005; Jop et al., 2006) proved much more convenient and efficient than more traditional approaches inspired by fluid mechanics (Campbell, 2006). Fig. 37 directly compares controlled normal stress to controlled volume measurements in a simulation of frictionless beads in slow steady shear flow with $I = 10^{-4}$, close to the quasistatic limit but with still notable differences in that case, as shown by Peyneau and Roux (2008a). For shear strain $\gamma < 1$, the normal stress is fixed ($\sigma_{22} = 1$ in the simulation units) while solid fraction Φ fluctuates, between 0.637 and 0.640 (slightly below the critical value), with average $\overline{\Phi} \simeq 0.6378$. For $\gamma > 1$, as Φ is now fixed to $\overline{\Phi}$, σ_{22} fluctuates between 0 and 4, so that measurement of an average stress is quite problematic. The second graph of Fig. 37 shows that the coefficient of internal friction, $\mu^* = |\sigma_{12}|/\sigma_{22}$, may be correctly identified in both situations.

Such an I-dependent coefficient of internal friction characterizes the material rheology, together with the I-dependent solid fraction. It should in principle be supplemented by measurements of normal stress differences ($\sigma_{22} - \sigma_{11}$ and $\sigma_{33} - \sigma_{22}$), which are usually quite small (Jop et al., 2006;

Khamseh et al., 2015). This defines what is now known as the "$\mu^*(I)$ rheology" (Jop et al., 2006; Forterre and Pouliquen, 2008; Andreotti et al., 2013) for dense granular flows.

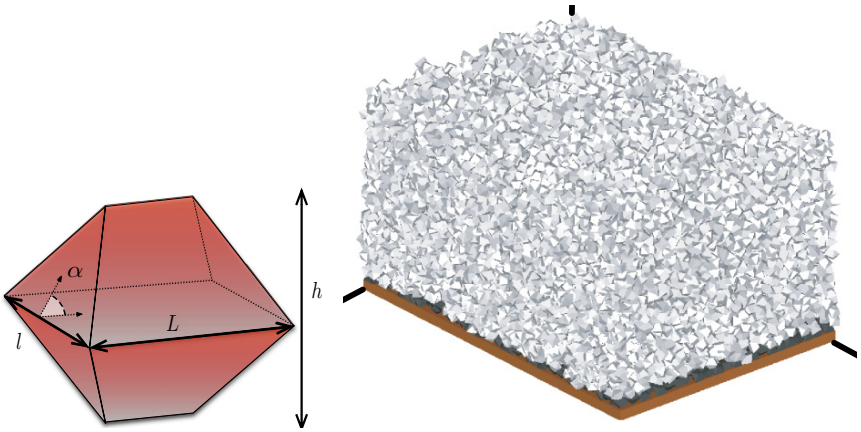

Figure 38. Left: one of the "pinacoids" used in study by Azéma et al. (2012). Right: sample (19000 such polyhedra) used in inclined plane flow.

Provided a steady state is achieved, with a uniform thickness, the flow, under gravity, of a granular layer down a plane inclined at angle ϕ with respect to a horizontal plane (with a rough surface, in order to avoid sliding), directly characterizes $\mu^*(I)$: the constant shear stress to normal stress (i.e., normal to the substrate or the free surface) ratio in the material fixes $\mu^*(I) = \tan\phi$. This has been applied experimentally (Jop et al., 2006) and

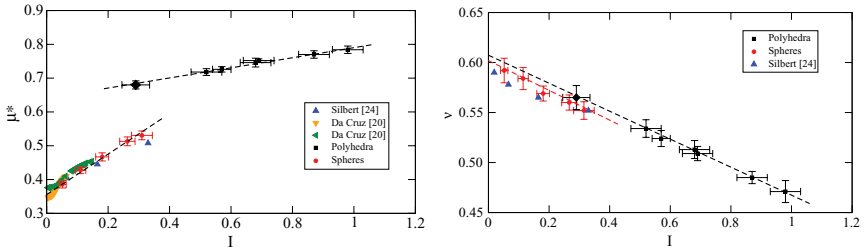

Figure 39. (Azéma et al., 2012) Left: $\mu^*(I)$ for polyhedra (upper curve) and spheres (bottom left, with comparisons with literature data). $\mu = 0.4$ for both shapes. Right: $\nu(I)$ $[= \Phi(I)]$ for polyhedra and spheres.

numerically, e.g. in the study by Azéma et al. (2012), for a certain type of polygons known as pinacoids, as shown in Fig. 38. The resulting functions $\mu^*(I)$ and $\Phi(I)$ are shown in Fig. 39, and compared to the results for spherical beads. The linear variation of functions $\mu^*(I)$ (increasing) and $\Phi(I)$ (decreasing) is often observed in range $I \sim 0.1$ (da Cruz et al., 2005; Forterre and Pouliquen, 2008), with a plateau of μ^* at larger values. For

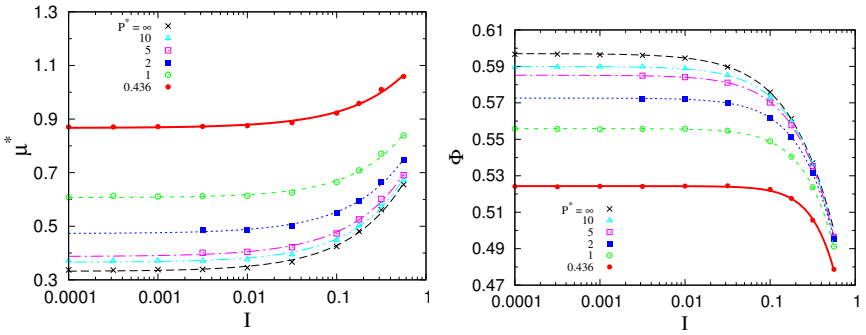

Figure 40. (Khamseh et al., 2015) $\mu^*(I)$ (left) and $\Phi(I)$ (right) for simulated dry (P^* infinite) and wet beads, for different P^*, defined using Eqs. 35 (with σ_{22} instead of P) and 6. Departures from $I \to 0$ limit fitted (solid lines) as power laws, with exponents near 0.7 for μ^* (whatever P^*), between 1 and 1.7 (depending on P^*) for Φ.

smaller I, as the quasistatic limit is approached the differences $\mu^*(I) - \mu_c^*$ and $\Phi_c - \Phi(I)$ with the quasistatic critical state values tend to vanish with different exponents (Hatano, 2007; Peyneau and Roux, 2008a). This is illustrated, for frictional ($\mu = 0.3$) bead assemblies, in Fig. 40 – which also contains results obtained for different P^* in systems endowed with capillary cohesion. The "$\mu^*(I)$ rheology" thus proves a robust constitutive approach. A particularly convincing illustration of its efficiency was supplied by Jop et al. (2006), who applied it to predict complex velocity profiles in surface flows of granular layers on top of static samples, between lateral walls. As the constitutive laws (suitably generalized to tensorial form) were initially measured in flow down inclined planes, this study involved no adjustable parameter.

An interesting development is the treatment of very dense suspensions with a similar approach, in which inertial number I is replaced by a "viscous number", $Vi = \eta\dot{\gamma}/P_p$, involving the normal stress P_p tranmitted to the solid particles (not to the whole suspension) and the viscosity η of the (Newtonian) suspending liquid (Cassar et al., 2005; Lemaître et al., 2009;

Boyer et al., 2011). This approach emphasizes the importance of frictional solid contacts in the rheology of very dense suspensions. The relevance of the same critical state as for dry grains in the quasistatic limit of $Vi \to 0$ implies in particular that the solid fraction at which the effective viscosity of the suspension diverges coincides with the critical state solid fraction Φ_c.

7 Concluding remarks

This incomplete tour of current research on micromechanical approaches to granular mechanics reveals first our enduring inability to predict some basic features of material behavior from grain-level phenomena: a quantitative determination of the properties of critical states, for instance, from particle geometry and intergranular friction coefficient, is still unavailable. Many difficulties are related to the complexity of packing geometry, and to how their force-carrying networks responds and rearranges under varying load. No such well-defined objects as crystal dislocation has been identified at the origin of granular plasticity. Some inspiration could be gained from recent advances in the modeling of the rheology of amorphous materials [see, e.g., Maloney and Lemaître (2006)], although two major features set granular materials apart: intergranular friction (the network properties are no longer expressible in terms of potential energy landscape), and very stiff interactions (causing singular behaviors linked to reduced hyperstaticity). Some useful classification of mechanical regimes and material states however emerge, such as type I versus type II strains, or well coordinated versus poorly coordinated systems. The fundamental concept of critical states, as first identified in macroscopic soil mechanics, proves a robust tool in granular material modeling, including in the presence of inertial and/or viscous effects. Current research perspectives are being pursued in the treatment of systems of growing complexity (with different grain shapes, different grain interactions, as for hard cohesive colloidal particles), but basic issues regarding the nature and microscopic origins of granular plasticity should still be investigated.

Bibliography

I. Agnolin and J.-N. Roux. Internal states of model isotropic granular packings. I. Assembling process, geometry, and contact networks. *Phys. Rev. E*, 76(6):061302, 2007a.

I. Agnolin and J.-N. Roux. Internal states of model isotropic granular packings. II. Compression and pressure cycles. *Phys. Rev. E*, 76(6):061303, 2007b.

I. Agnolin and J.-N. Roux. Internal states of model isotropic granular packings. III. Elastic properties. *Phys. Rev. E*, 76(6):061304, 2007c.

B. Andreotti, Y. Forterre, and O. Pouliquen. *Granular Media: Between Fluid and Solid*. Cambridge University Press, Cambridge, UK, 2013.

N. W. Ashcroft, N. D. Mermin, and D. Wei. *Solid State Physics*. Cengage Learning Asia, 2016.

T. Aste and D. Weaire. *The Pursuit of Perfect Packing*. Institute of Physics Publishing, Bristol, 2000.

T. Aste, M. Saadatfar, and T. J. Senden. The geometrical structure of disordered sphere packings. *Phys. Rev. E*, 71:061302, 2005.

É. Azéma and F. Radjaï. Internal struture of inertial granular flows. *Phys. Rev. Lett.*, 112:078001, 2014.

É. Azéma, F. Radjaï, and G. Saussine. Quasistatic rheology, force transmission and fabric properties of a packing of irregular polyhedral particles. *Mechanics of Materials*, 41:729–741, 2009.

É. Azéma, Y. Descantes, N. Roquet, J.-N. Roux, and F. Chevoir. Discrete simulation of dense flows of polyhedral grains down a rough inclined plane. *Phys. Rev. E*, 86:031303, 2012.

É. Azéma, F. Radjaï, and F. Dubois. Packings of irregular polyhedral particles: Strength, structure, and effects of angularity. *Phys. Rev. E*, 87: 062223, 2013.

É. Azéma, F. Radjaï, and J.-N. Roux. Internal friction and absence of dilatancy of packings of frictionless polygons. *Phys. Rev. E*, 91:010202(R), 2015.

T. Baumberger and C. Caroli. Solid friction, from stick-slip down to pinning and aging. *Advances in Physics*, 55:279–348, 2006.

N. Benahmed, J. Canou, and J.-C. Dupla. Structure initiale et propriétés de liquéfaction statique d'un sable. *Comptes-Rendus Académie des Sciences, Mécanique*, 332:887–894, 2004.

F. P. Bowden and D. Tabor. *The Friction and Lubrication of Solids*, volume I. Clarendon Press, Oxford, 1950.

F. Boyer, É. Guazzelli, and O. Pouliquen. Unifying suspension and granular rheology. *Phys. Rev. Lett.*, 107:188301:1–5, 2011.

N. V. Brilliantov and T. Pöschel. Collision of adhesive viscoelastic particles. In H. Hinrichsen and D. E. Wolf, editors, *The Physics of Granular Media*, pages 189–209, Berlin, 2004. Wiley-VCH.

C. S. Campbell. Granular material flows – an overview. *Powder Technology*, 162:208–229, 2006.

C. Cassar, M. Nicolas, and O. Pouliquen. Submarine granular flows down inclined plane. *Phys. Fluids*, 17, 2005.

A. Castellanos. The relationship between attractive interparticle forces and bulk behaviour in dry and uncharged fine powders. *Advances in Physics*, 54:263–376, 2005.

P. Chaudhuri, L. Berthier, and S. Sastry. Jamming Transitions in Amorphous Packings of Frictionless Spheres Occur over a Continuous Range of Volume Fractions. *Phys. Rev. Lett.*, 104:165701, 2010.

J. Christoffersen, M. M. Mehrabadi, and S. Nemat-Nasser. A micromechanical description of granular material behavior. *Journal of Applied Mechanics*, 48:339–344, 1981.

G. Combe and J.-N. Roux. Strain versus stress in a model granular material: a devil's staircase. *Phys. Rev. Lett.*, 85:3628–3631, 2000.

G. Combe and J.-N. Roux. Construction of Granular Assemblies under Satic Loading. In *Discrete-element Modeling of Granular Materials* Radjaï and Dubois (2011), chapter 6, pages 153–180.

S. N. Coppersmith, C. H. Liu, S. Majumdar, O. Narayan, and T. A. Witten. Model for force fluctuations in bead packs. *Phys. Rev. E*, 53:4673–4685, 1996.

F. da Cruz, S. Emam, M. Prochnow, J.-N. Roux, and F. Chevoir. Rheophysics of dense granular materials: discrete simulation of plane shear flows. *Phys. Rev. E*, 72:021309, 2005.

R. Deluzarche and B. Cambou. Discrete numerical modelling of rockfill dams. *International for numerical and analytical methods in geomechanics*, 30:1075–1096, 2006.

H. di Benedetto, T. Doanh, H. Geoffroy, and C. Sauzéat, editors. *Deformation characteristics of geomaterials: Recent investigations and prospects*, Lisse, 2003. Swets and Zeitlinger.

A. Donev, R. Connelly, F. H. Stillinger, and S. Torquato. Hypostatic Jammed Packings of Nonspherical Hard Particles: Ellipses and Ellipsoids. *Phys. Rev. E*, 75:051304, 2007.

D. Elata and J. G. Berryman. Contact force-displacement laws and the mechanical behavior of random packs of identical spheres. *Mechanics of Materials*, 24:229–240, 1996.

S. Emam, J.-N. Roux, J. Canou, A. Corfdir, and J.-C. Dupla. Granular packings assembled by rain deposition: an experimental and numerical study. In R. García Rojo, H. J. Herrmann, and S. McNamara, editors, *Powders and Grains 2005*, pages 49–52, Leiden, 2005. Balkema.

N. Estrada, É. Azéma, F. Radjaï, and A. Taboada. Identification of rolling resistance as a shape parameter in sheared granular media. *Phys. Rev. E*, 84:011306, 2011.

Y. Forterre and O. Pouliquen. Flows of dense granular media. *Annu. Rev. Fluid Mech.*, 40:1–24, 2008.

GDR MiDi. On dense granular flows. *European Physical Journal E*, 14: 341–365, 2004.

F. A. Gilabert, J.-N. Roux, and A. Castellanos. Computer simulation of model cohesive powders: Influence of assembling procedure and contact laws on low consolidation states. *Phys. Rev. E*, 75(1):011303, 2007.

J. D. Goddard and A. K. Didwania. Computations of dilatancy and yield surfaces for assemblies of rigid frictional spheres. *Quarterly Journal of Mechanics and Applied Mathematics*, 51:15–43, 1998.

T. Hatano. Power-law friction in closely packed granular materials. *Phys. Rev. E*, 75:060301(R), 2007.

J. N. Israelashvili. *Intermolecular and Surface Forces*. Academic Press, 1991.

K. Iwashita and M. Oda. *Mechanics of Granular Materials: An Introduction*. Taylor & Francis, Netherlands, 1999.

H. M. Jaeger, S. R. Nagel, and R. P. Behringer. Granular solids, liquids, and gases. *Rev. Mod. Phys.*, 68(4):1259–1273, 1996.

X. Jia, C. Caroli, and B. Velický. Ultrasound propagation in externally stressed granular media. *Phys. Rev. Lett.*, 82:1863–1866, 1999.

K. L. Johnson. *Contact Mechanics*. Cambridge University Press, 1985.

P. Jop, Y. Forterre, and O. Pouliquen. A constitutive law for dense granular flow. *Nature*, 441:727–730, 2006.

M. H. Khalili, J.-N. Roux, J.-M. Pereira, S. Brisard, and M. Bornert. A numerical study of one-dimensional compression of granular materials: I. Stress-strain behavior, microstructure and irreversibility. *Phys. Rev. E*, 95(032907), 2017.

S. Khamseh, J.-N. Roux, and F. Chevoir. Flow of wet granular materials: a numerical study. *Phys. Rev. E*, 92:022201, 2015.

M. R. Kuhn. Structured deformation in granular materials. *Mechanics of Materials*, 31:407–429, 1999.

M. R. Kuhn and C. S. Chang. Stability, Bifurcation and Softening in Discrete Systems: A Conceptual Approach for Granular Materials. *International Journal of Solids and Structures*, 43:6026–6051, 2006.

R. Kuwano and R. J. Jardine. On the applicability of cross-anisotropic elasticity to granular materials at very small strains. *Géotechnique*, 52: 727–749, 2002.

L. La Ragione and J. T. Jenkins. The initial response of an idealized granular material. *Proceedings of the Royal Society A*, 63(2079):735–758, 2007. ISSN 1364-5021.

P. V. Lade and J. M. Duncan. Elastoplastic stress-strain theory for cohesionless soil. *J. Geotech. Eng. Div.*, 101:1037–1053, 1975.

A. Lemaître, J.-N. Roux, and F. Chevoir. What do dry granular flows tell us about dense non-brownian suspension rheology? *Rheologica Acta*, 48: 925–942, 2009.

G. Lian, C. Thornton, and M. J. Adams. A theoretical study of the liquid bridge forces between two rigid spherical bodies. *J. of Colloid and Interface Sci.*, 161(1):138–147, 1993.

C. E. Maloney and A. Lemaître. Amorphous systems in athermal, quasistatic shear. *Phys. Rev. E*, 74:016118, 2006.

M. T. Manzani and Y. F. Dafalias. A critical state two-surface plasticity model for sands. *Géotechnique*, 47(2):255–272, 1997.

D. Maugis. *Contact, adhesion and rupture of elastic solids*. Springer, Berlin, 2000.

N. Maw, J. R. Barber, and J. N. Fawcett. Oblique impact of elastic spheres. *Wear*, 38(1):101–114, 1976.

S. McNamara and H. J. Herrmann. Quasirigidity: some uniqueness issues. *Phys. Rev. E*, 74:061303, 2006.

R. D. Mindlin and H. Deresiewicz. Elastic spheres in contact under varying oblique forces. *ASME Journal of Applied Mechanics*, 20:327–340, 1953.

J. K. Mitchell and K. Soga. *Fundamentals of Soil Behavior*. Wiley, 2005.

R. M. Nedderman. *Statics and Kinetics of Granular Materials*. Cambridge University Press, Cambridge, UK, 1992.

S. Nemat-Nasser and M. Hori. *Micromechanics. Overall properties of heterogeneous materials.* North-Holland, 1993.

C. O'Hern, L. E. Silbert, A. J. Liu, and S. R. Nagel. Jamming at zero temperature and zero applied stress: The epitome of disorder. *Phys. Rev. E*, 68(1):011306, 2003.

C. O'Sullivan. *Particulate discrete element modeling, a geomechanics perspective*. Spon Press, London, 2011.

P.-E. Peyneau and J.-N. Roux. Frictionless bead packs have macroscopic friction, but no dilatancy. *Phys. Rev. E*, 78:011307, 2008a.

P.-E. Peyneau and J.-N. Roux. Solidlike behavior and anisotropy in rigid frictionless bead assemblies. *Phys. Rev. E*, 78:041307, 2008b.

O. Pitois, P. Moucheront, and X. Chateau. Liquid bridge between two moving spheres: An experimental study of viscosity effects. *J. Coll. Interf. Sci.*, 231:26–31, 2000.

N. S. Rad and M. T. Tumay. Factors affecting sand specimen preparation by raining. *ASTM Journal of Geotechnical Testing*, 10:31–37, 1987.

F. Radjaï. Modeling force transmission in granular materials. *Comptes Rendus Physique*, 16(1):3–9, 2015.

F. Radjaï and F. Dubois. *Discrete-element modeling of granular materials*. Wiley, 2011.

F. Radjaï and V. Richefeu. Bond anisotropy and cohesion of wet granular materials. *Phil. Trans. R. Soc. A*, 367:5123–5138, 2009.
F. Radjaï and V. Richefeu. Contact dynamics as a nonsmooth discrete element method. *Mechanics of Materials*, 41:715–728, 2009.
F. Radjaï and S. Roux. Turbulentlike fluctuations in quasistatic flow of granular media. *Phys. Rev. Lett.*, 89(6):064302, 2002.
F. Radjaï, D. E. Wolf, M. Jean, and J.-J. Moreau. Bimodal character of stress transmission in granular packings. *Phys. Rev. Lett.*, 80:61–64, 1998.
F. Radjaï, S. Nezamabadi, S. Luding, and J.-Y. Delenne, editors. *Powders and Grains 2017*, number 140 in EPJ Web of Conferences, 2017. EDP Sciences.
R. Ramirez, T. Pöschel, N. V. Brilliantov, and T. Schwager. Coefficient of restitution of colliding viscoelastic spheres. *Phys. Rev. E*, 60:4465–4472, 1999.
O. Reynolds. On the dilatancy of media composed of rigid particles in contact. *Philosophical Magazine (5th series)*, 20:469–481, 1885.
D. Richard, I. Iordanoff, Y. Berthier, M. Renouf, and N. Fillot. Friction coefficient as a macroscopic view of local dissipation. *Journal of Tribology – Transactions of the ASME*, 129:829–835, 2007.
J.-N. Roux. Geometric origin of mechanical properties of granular materials. *Phys. Rev. E*, 61:6802–6836, 2000.
J.-N. Roux. Pre-peak deformation of model granular materials: A DEM study. In K. Soga, K. Kumar, G. Biscontin, and M. Kuo, editors, *Geomechanics from micro to macro*, pages 49–54. CRC-Press-Taylor & Francis, 2015.
J.-N. Roux and F. Chevoir. Dimensional Analysis and Control Parameters. In *Discrete-element Modeling of Granular Materials* Radjaï and Dubois (2011), chapter 8, pages 199–232.
J.-N. Roux and G. Combe. Quasistatic rheology and the origins of strain. *C. R. Physique*, 3:131–140, 2002.
J.-N. Roux and G. Combe. How granular materials deform in quasistatic conditions. In J. D. Goddard, J. T. Jenkins, and P. Giovine, editors, *IUTAM-ISIMM Symposium on mathematical modeling and physical instances of granular flow*, volume 1227 of *AIP Conference Proceedings*, page 260, 2010.
J.-N. Roux and G. Combe. Quasi-Static Methods. In *Discrete-element Modeling of Granular Materials* Radjaï and Dubois (2011), chapter 3, pages 67–101.
P. Sánchez, D. Scheeres, M. Hirabayashi, and S. Tardivel. Looking into the evolution of granular asteroids in the Solar System. In Radjaï et al. (2017), page 14004.

L. E. Silbert, D. Ertaş, G. S. Grest, T. C. Halsey, and D. Levine. Geometry of frictionless and frictional sphere packings. *Phys. Rev. E*, 65(3):031304, 2002.

S. Somfai, M. van Hecke, W. G. Ellenbroek, K. Shundyak, and W. van Saarloos. Critical and noncritical jamming of frictional grains. *Phys. Rev. E*, 75(2):020301, 2007.

A. S. J. Suiker and N. A. Fleck. Frictional collapse of granular assemblies. *ASME Journal of Applied Mechanics*, 71:350–358, 2004.

G. Szpiro. *Kepler's conjecture*. Wiley, 2003.

F. Tatsuoka. Impacts on geotechnical engineering of several recent findings from laboratory stress-strain tests on geomaterials. In G. Correia and H. Brandle, editors, *Geotechnics for roads, rail tracks and earth structures*, pages 69–140, Lisse, 2001. Balkema.

V.-D. Than. *Compression behavior of loose wet granular materials: experiments and discrete numerical simulations.* PhD thesis, Université Paris Est, 2017.

V.-D. Than, S. Khamseh, A.-M. Tang, J.-M. Pereira, F. Chevoir, and J.-N. Roux. Basic Mechanical Properties of Wet Granular Materials: A DEM Study. *ASCE J. Eng. Mech.*, 143(SI1):C4016001, 2017.

M. F. Thorpe and P. M. Duxbury, editors. *Rigidity Theory and Applications*, Fundamental Materials Research, 1998. Kluwer Academic.

C. Voivret, F. Radjaï, J.-Y. Delenne, and M.S. El Youssoufi. Multiscale force networks in highly polydisperse granular media. *Phys. Rev. Lett.*, 102:178001, 2009.

I. Volkov, M. Cieplak, J. Koplik, and J. R. Banavar. Molecular dynamics simulations of crystallization of hard spheres. *Phys. Rev. E*, 66(6):061401, 2002.

P. R. Welker and S. C. McNamara. What triggers failure in frictional granular assemblies? *Phys. Rev. E*, 79:061305, 2009.

D. M. Wood. *Soil Behaviour and Critical State Soil Mechanics*. Cambridge University Press, 1990.

M. Wyart. On the rigidity of amorphous solids. *Annales de Physique Fr.*, 30:1–96, 2006.

Bibliography

I. Agnolin and J.-N. Roux. Internal states of model isotropic granular packings. I. Assembling process, geometry, and contact networks. *Phys. Rev. E*, 76(6):061302, 2007a.

I. Agnolin and J.-N. Roux. Internal states of model isotropic granular packings. II. Compression and pressure cycles. *Phys. Rev. E*, 76(6):061303, 2007b.

I. Agnolin and J.-N. Roux. Internal states of model isotropic granular packings. III. Elastic properties. *Phys. Rev. E*, 76(6):061304, 2007c.

B. Andreotti, Y. Forterre, and O. Pouliquen. *Granular Media: Between Fluid and Solid*. Cambridge University Press, Cambridge, UK, 2013.

N. W. Ashcroft, N. D. Mermin, and D. Wei. *Solid State Physics*. Cengage Learning Asia, 2016.

T. Aste and D. Weaire. *The Pursuit of Perfect Packing*. Institute of Physics Publishing, Bristol, 2000.

T. Aste, M. Saadatfar, and T. J. Senden. The geometrical structure of disordered sphere packings. *Phys. Rev. E*, 71:061302, 2005.

É. Azéma and F. Radjaï. Internal struture of inertial granular flows. *Phys. Rev. Lett.*, 112:078001, 2014.

É. Azéma, F. Radjaï, and G. Saussine. Quasistatic rheology, force transmission and fabric properties of a packing of irregular polyhedral particles. *Mechanics of Materials*, 41:729–741, 2009.

É. Azéma, Y. Descantes, N. Roquet, J.-N. Roux, and F. Chevoir. Discrete simulation of dense flows of polyhedral grains down a rough inclined plane. *Phys. Rev. E*, 86:031303, 2012.

É. Azéma, F. Radjaï, and F. Dubois. Packings of irregular polyhedral particles: Strength, structure, and effects of angularity. *Phys. Rev. E*, 87: 062223, 2013.

É. Azéma, F. Radjaï, and J.-N. Roux. Internal friction and absence of dilatancy of packings of frictionless polygons. *Phys. Rev. E*, 91:010202(R), 2015.

T. Baumberger and C. Caroli. Solid friction, from stick-slip down to pinning and aging. *Advances in Physics*, 55:279–348, 2006.

N. Benahmed, J. Canou, and J.-C. Dupla. Structure initiale et propriétés de liquéfaction statique d'un sable. *Comptes-Rendus Académie des Sciences, Mécanique*, 332:887–894, 2004.

F. P. Bowden and D. Tabor. *The Friction and Lubrication of Solids*, volume I. Clarendon Press, Oxford, 1950.

F. Boyer, É. Guazzelli, and O. Pouliquen. Unifying suspension and granular rheology. *Phys. Rev. Lett.*, 107:188301:1–5, 2011.

N. V. Brilliantov and T. Pöschel. Collision of adhesive viscoelastic particles. In H. Hinrichsen and D. E. Wolf, editors, *The Physics of Granular Media*, pages 189–209, Berlin, 2004. Wiley-VCH.

C. S. Campbell. Granular material flows – an overview. *Powder Technology*, 162:208–229, 2006.

C. Cassar, M. Nicolas, and O. Pouliquen. Submarine granular flows down inclined plane. *Phys. Fluids*, 17, 2005.

A. Castellanos. The relationship between attractive interparticle forces and bulk behaviour in dry and uncharged fine powders. *Advances in Physics*, 54:263–376, 2005.

P. Chaudhuri, L. Berthier, and S. Sastry. Jamming Transitions in Amorphous Packings of Frictionless Spheres Occur over a Continuous Range of Volume Fractions. *Phys. Rev. Lett.*, 104:165701, 2010.

J. Christoffersen, M. M. Mehrabadi, and S. Nemat-Nasser. A micromechanical description of granular material behavior. *Journal of Applied Mechanics*, 48:339–344, 1981.

G. Combe and J.-N. Roux. Strain versus stress in a model granular material: a devil's staircase. *Phys. Rev. Lett.*, 85:3628–3631, 2000.

G. Combe and J.-N. Roux. Construction of Granular Assemblies under Satic Loading. In *Discrete-element Modeling of Granular Materials* Radjaï and Dubois (2011), chapter 6, pages 153–180.

S. N. Coppersmith, C. H. Liu, S. Majumdar, O. Narayan, and T. A. Witten. Model for force fluctuations in bead packs. *Phys. Rev. E*, 53:4673–4685, 1996.

F. da Cruz, S. Emam, M. Prochnow, J.-N. Roux, and F. Chevoir. Rheophysics of dense granular materials: discrete simulation of plane shear flows. *Phys. Rev. E*, 72:021309, 2005.

R. Deluzarche and B. Cambou. Discrete numerical modelling of rockfill dams. *International for numerical and analytical methods in geomechanics*, 30:1075–1096, 2006.

H. di Benedetto, T. Doanh, H. Geoffroy, and C. Sauzéat, editors. *Deformation characteristics of geomaterials: Recent investigations and prospects*, Lisse, 2003. Swets and Zeitlinger.

A. Donev, R. Connelly, F. H. Stillinger, and S. Torquato. Hypostatic Jammed Packings of Nonspherical Hard Particles: Ellipses and Ellipsoids. *Phys. Rev. E*, 75:051304, 2007.

D. Elata and J. G. Berryman. Contact force-displacement laws and the mechanical behavior of random packs of identical spheres. *Mechanics of Materials*, 24:229–240, 1996.

S. Emam, J.-N. Roux, J. Canou, A. Corfdir, and J.-C. Dupla. Granular packings assembled by rain deposition: an experimental and numerical study. In R. García Rojo, H. J. Herrmann, and S. McNamara, editors, *Powders and Grains 2005*, pages 49–52, Leiden, 2005. Balkema.

N. Estrada, É. Azéma, F. Radjaï, and A. Taboada. Identification of rolling resistance as a shape parameter in sheared granular media. *Phys. Rev. E*, 84:011306, 2011.

Y. Forterre and O. Pouliquen. Flows of dense granular media. *Annu. Rev. Fluid Mech.*, 40:1–24, 2008.

GDR MiDi. On dense granular flows. *European Physical Journal E*, 14: 341–365, 2004.

F. A. Gilabert, J.-N. Roux, and A. Castellanos. Computer simulation of model cohesive powders: Influence of assembling procedure and contact laws on low consolidation states. *Phys. Rev. E*, 75(1):011303, 2007.

J. D. Goddard and A. K. Didwania. Computations of dilatancy and yield surfaces for assemblies of rigid frictional spheres. *Quarterly Journal of Mechanics and Applied Mathematics*, 51:15–43, 1998.

T. Hatano. Power-law friction in closely packed granular materials. *Phys. Rev. E*, 75:060301(R), 2007.

J. N. Israelashvili. *Intermolecular and Surface Forces*. Academic Press, 1991.

K. Iwashita and M. Oda. *Mechanics of Granular Materials: An Introduction*. Taylor & Francis, Netherlands, 1999.

H. M. Jaeger, S. R. Nagel, and R. P. Behringer. Granular solids, liquids, and gases. *Rev. Mod. Phys.*, 68(4):1259–1273, 1996.

X. Jia, C. Caroli, and B. Velický. Ultrasound propagation in externally stressed granular media. *Phys. Rev. Lett.*, 82:1863–1866, 1999.

K. L. Johnson. *Contact Mechanics*. Cambridge University Press, 1985.

P. Jop, Y. Forterre, and O. Pouliquen. A constitutive law for dense granular flow. *Nature*, 441:727–730, 2006.

M. H. Khalili, J.-N. Roux, J.-M. Pereira, S. Brisard, and M. Bornert. A numerical study of one-dimensional compression of granular materials: I. Stress-strain behavior, microstructure and irreversibility. *Phys. Rev. E*, 95(032907), 2017.

S. Khamseh, J.-N. Roux, and F. Chevoir. Flow of wet granular materials: a numerical study. *Phys. Rev. E*, 92:022201, 2015.

M. R. Kuhn. Structured deformation in granular materials. *Mechanics of Materials*, 31:407–429, 1999.

M. R. Kuhn and C. S. Chang. Stability, Bifurcation and Softening in Discrete Systems: A Conceptual Approach for Granular Materials. *International Journal of Solids and Structures*, 43:6026–6051, 2006.

R. Kuwano and R. J. Jardine. On the applicability of cross-anisotropic elasticity to granular materials at very small strains. *Géotechnique*, 52: 727–749, 2002.

L. La Ragione and J. T. Jenkins. The initial response of an idealized granular material. *Proceedings of the Royal Society A*, 63(2079):735–758, 2007. ISSN 1364-5021.

P. V. Lade and J. M. Duncan. Elastoplastic stress-strain theory for cohesionless soil. *J. Geotech. Eng. Div.*, 101:1037–1053, 1975.

A. Lemaître, J.-N. Roux, and F. Chevoir. What do dry granular flows tell us about dense non-brownian suspension rheology? *Rheologica Acta*, 48: 925–942, 2009.

G. Lian, C. Thornton, and M. J. Adams. A theoretical study of the liquid bridge forces between two rigid spherical bodies. *J. of Colloid and Interface Sci.*, 161(1):138–147, 1993.

C. E. Maloney and A. Lemaître. Amorphous systems in athermal, quasistatic shear. *Phys. Rev. E*, 74:016118, 2006.

M. T. Manzani and Y. F. Dafalias. A critical state two-surface plasticity model for sands. *Géotechnique*, 47(2):255–272, 1997.

D. Maugis. *Contact, adhesion and rupture of elastic solids*. Springer, Berlin, 2000.

N. Maw, J. R. Barber, and J. N. Fawcett. Oblique impact of elastic spheres. *Wear*, 38(1):101–114, 1976.

S. McNamara and H. J. Herrmann. Quasirigidity: some uniqueness issues. *Phys. Rev. E*, 74:061303, 2006.

R. D. Mindlin and H. Deresiewicz. Elastic spheres in contact under varying oblique forces. *ASME Journal of Applied Mechanics*, 20:327–340, 1953.

J. K. Mitchell and K. Soga. *Fundamentals of Soil Behavior*. Wiley, 2005.

R. M. Nedderman. *Statics and Kinetics of Granular Materials*. Cambridge University Press, Cambridge, UK, 1992.

S. Nemat-Nasser and M. Hori. *Micromechanics. Overall properties of heterogeneous materials*. North-Holland, 1993.

C. O'Hern, L. E. Silbert, A. J. Liu, and S. R. Nagel. Jamming at zero temperature and zero applied stress: The epitome of disorder. *Phys. Rev. E*, 68(1):011306, 2003.

C. O'Sullivan. *Particulate discrete element modeling, a geomechanics perspective*. Spon Press, London, 2011.

P.-E. Peyneau and J.-N. Roux. Frictionless bead packs have macroscopic friction, but no dilatancy. *Phys. Rev. E*, 78:011307, 2008a.

P.-E. Peyneau and J.-N. Roux. Solidlike behavior and anisotropy in rigid frictionless bead assemblies. *Phys. Rev. E*, 78:041307, 2008b.

O. Pitois, P. Moucheront, and X. Chateau. Liquid bridge between two moving spheres: An experimental study of viscosity effects. *J. Coll. Interf. Sci.*, 231:26–31, 2000.

N. S. Rad and M. T. Tumay. Factors affecting sand specimen preparation by raining. *ASTM Journal of Geotechnical Testing*, 10:31–37, 1987.

F. Radjaï. Modeling force transmission in granular materials. *Comptes Rendus Physique*, 16(1):3–9, 2015.

F. Radjaï and F. Dubois. *Discrete-element modeling of granular materials*. Wiley, 2011.

F. Radjaï and V. Richefeu. Bond anisotropy and cohesion of wet granular materials. *Phil. Trans. R. Soc. A*, 367:5123–5138, 2009.
F. Radjaï and V. Richefeu. Contact dynamics as a nonsmooth discrete element method. *Mechanics of Materials*, 41:715–728, 2009.
F. Radjaï and S. Roux. Turbulentlike fluctuations in quasistatic flow of granular media. *Phys. Rev. Lett.*, 89(6):064302, 2002.
F. Radjaï, D. E. Wolf, M. Jean, and J.-J. Moreau. Bimodal character of stress transmission in granular packings. *Phys. Rev. Lett.*, 80:61–64, 1998.
F. Radjaï, S. Nezamabadi, S. Luding, and J.-Y. Delenne, editors. *Powders and Grains 2017*, number 140 in EPJ Web of Conferences, 2017. EDP Sciences.
R. Ramirez, T. Pöschel, N. V. Brilliantov, and T. Schwager. Coefficient of restitution of colliding viscoelastic spheres. *Phys. Rev. E*, 60:4465–4472, 1999.
O. Reynolds. On the dilatancy of media composed of rigid particles in contact. *Philosophical Magazine (5th series)*, 20:469–481, 1885.
D. Richard, I. Iordanoff, Y. Berthier, M. Renouf, and N. Fillot. Friction coefficient as a macroscopic view of local dissipation. *Journal of Tribology – Transactions of the ASME*, 129:829–835, 2007.
J.-N. Roux. Geometric origin of mechanical properties of granular materials. *Phys. Rev. E*, 61:6802–6836, 2000.
J.-N. Roux. Pre-peak deformation of model granular materials: A DEM study. In K. Soga, K. Kumar, G. Biscontin, and M. Kuo, editors, *Geomechanics from micro to macro*, pages 49–54. CRC-Press-Taylor & Francis, 2015.
J.-N. Roux and F. Chevoir. Dimensional Analysis and Control Parameters. In *Discrete-element Modeling of Granular Materials* Radjaï and Dubois (2011), chapter 8, pages 199–232.
J.-N. Roux and G. Combe. Quasistatic rheology and the origins of strain. *C. R. Physique*, 3:131–140, 2002.
J.-N. Roux and G. Combe. How granular materials deform in quasistatic conditions. In J. D. Goddard, J. T. Jenkins, and P. Giovine, editors, *IUTAM-ISIMM Symposium on mathematical modeling and physical instances of granular flow*, volume 1227 of *AIP Conference Proceedings*, page 260, 2010.
J.-N. Roux and G. Combe. Quasi-Static Methods. In *Discrete-element Modeling of Granular Materials* Radjaï and Dubois (2011), chapter 3, pages 67–101.
P. Sánchez, D. Scheeres, M. Hirabayashi, and S. Tardivel. Looking into the evolution of granular asteroids in the Solar System. In Radjaï et al. (2017), page 14004.

L. E. Silbert, D. Ertaş, G. S. Grest, T. C. Halsey, and D. Levine. Geometry of frictionless and frictional sphere packings. *Phys. Rev. E*, 65(3):031304, 2002.

S. Somfai, M. van Hecke, W. G. Ellenbroek, K. Shundyak, and W. van Saarloos. Critical and noncritical jamming of frictional grains. *Phys. Rev. E*, 75(2):020301, 2007.

A. S. J. Suiker and N. A. Fleck. Frictional collapse of granular assemblies. *ASME Journal of Applied Mechanics*, 71:350–358, 2004.

G. Szpiro. *Kepler's conjecture*. Wiley, 2003.

F. Tatsuoka. Impacts on geotechnical engineering of several recent findings from laboratory stress-strain tests on geomaterials. In G. Correia and H. Brandle, editors, *Geotechnics for roads, rail tracks and earth structures*, pages 69–140, Lisse, 2001. Balkema.

V.-D. Than. *Compression behavior of loose wet granular materials: experiments and discrete numerical simulations.* PhD thesis, Université Paris Est, 2017.

V.-D. Than, S. Khamseh, A.-M. Tang, J.-M. Pereira, F. Chevoir, and J.-N. Roux. Basic Mechanical Properties of Wet Granular Materials: A DEM Study. *ASCE J. Eng. Mech.*, 143(SI1):C4016001, 2017.

M. F. Thorpe and P. M. Duxbury, editors. *Rigidity Theory and Applications*, Fundamental Materials Research, 1998. Kluwer Academic.

C. Voivret, F. Radjaï, J.-Y. Delenne, and M.S. El Youssoufi. Multiscale force networks in highly polydisperse granular media. *Phys. Rev. Lett.*, 102:178001, 2009.

I. Volkov, M. Cieplak, J. Koplik, and J. R. Banavar. Molecular dynamics simulations of crystallization of hard spheres. *Phys. Rev. E*, 66(6):061401, 2002.

P. R. Welker and S. C. McNamara. What triggers failure in frictional granular assemblies? *Phys. Rev. E*, 79:061305, 2009.

D. M. Wood. *Soil Behaviour and Critical State Soil Mechanics*. Cambridge University Press, 1990.

M. Wyart. On the rigidity of amorphous solids. *Annales de Physique Fr.*, 30:1–96, 2006.